

# Complex structures of boson stars and anisotropic distribution of satellite galaxies

Víctor Jaramillo<sup>1,2,\*</sup> and Shuang-Yong Zhou<sup>3,2,4,†</sup>

<sup>1</sup>*Department of Astronomy, University of Science and Technology of China, Hefei, Anhui 230026, China*

<sup>2</sup>*Department of Modern Physics, University of Science and Technology of China, Hefei 230026, China*

<sup>3</sup>*Interdisciplinary Center for Theoretical Study, University of Science and Technology of China, Hefei, Anhui 230026, China*

<sup>4</sup>*Peng Huanwu Center for Fundamental Theory, Hefei, Anhui 230026, China*

(Dated: Wednesday 4<sup>th</sup> December, 2024)

We construct and explore the complex structures of boson stars, drawing inspiration from similar configurations of non-topological solitons in Minkowski space. These “molecular states” of boson stars have a multipolar structure and both positive and negative Noether charges within one star, and the opposite charges swap with time. Thanks to the gravitational attraction, they exist even in the case of a free scalar field. We also explore the effects of scalar self-interactions on these complex structures. We propose to use galactic-scale charge-swapping boson stars as a potential solution to the problem of the observed anisotropic distribution of satellite galaxies.

## CONTENTS

I. Introduction	1
II. Theory and setup	2
A. 3+1 decomposition	4
B. Stationary isolated boson btars	4
C. Units and scales	5
D. Preparing complex boson stars: solving initial constraints	6
III. Free scalar	9
A. Dipolar (charge-swapping) boson star	9
B. Higher multipolar boson stars	12
IV. Self-interacting scalar	14
A. Sextic potential	14
B. Logarithmic potential	17
V. Anisotropic distribution of satellite galaxies	18
VI. Conclusions	22
Acknowledgments	24
Appendix: Convergence tests	24
References	25

## I. INTRODUCTION

Boson stars are nowadays well known solutions that arise in the context of complex scalar fields coupled to Einstein gravity. The first such self-gravitating, spatially localized, stationary configurations were obtained more

than 50 years ago [1]. This particular nonlinear solution, which nowadays is known as a mini-boson star, arise within the simplest model of a minimally coupled free scalar field and when spherical symmetry is assumed. Self-interactions such as the quartic [2] and sextic [3] terms in the scalar potential enrich the family of boson stars. The variety of boson stars that can be found in the literature goes beyond modifications to the scalar potential, see e.g. [4] for a generalization including electrically charged scalar fields, [5] for solutions with horizons, [6] for solutions of a vectorial bosonic field and some others to which we will refer later. However, many of them (and in particular the self-interacting ones) share similar dynamical properties with the mini-boson stars (see [7] for a review on this topic and [8] for an unified view in the nonrelativistic limit), the most important of which include the stability and existence of a formation mechanism [9–26]. This has enabled boson stars to find applications in various astrophysical and cosmological scenarios [27–42]

Stationary boson stars beyond spherical symmetry have also been studied for quite a long time. Among them are the (stationary) spinning boson stars [43], which have a toroidal topology and are unstable [44] unless self-interactions are included [45, 46]. Another example is that of (static) dipolar boson stars [47]. These solutions are balanced by the attraction of gravity and the repulsion of the two blobs, which possess the same value and sign of the Noether charge but with a  $\pi$  relative phase. They have been revisited recently in [48, 49] and again, appear to be stabilized only when self-interactions are included [50]. Beyond these two cases, there are the chains of boson stars, constructed naturally with self-interactions [51, 52] and interestingly also without them [53, 54]. Additionally, there can be static (in terms of the spacetime metric) multipolar boson stars [55] which contain both dipolar components and chain components in addition to some non-axisymmetric structure, with the overall morphology of the energy density akin to the orbitals of the hydrogen atom. As the dipolar boson stars

\* [jaramillo@ustc.edu.cn](mailto:jaramillo@ustc.edu.cn)

† [zhoushy@ustc.edu.cn](mailto:zhoushy@ustc.edu.cn)

and chains of stars, the general multipolar case has a nonzero total Noether charge and every multipolar component contributes to the total charge with densities of the same sign.

Furthermore, boson star solutions by coupling multiple fields to gravity have also been discussed. On the one hand, stationary non-trivial solutions in the free-field case have been obtained in [56] where the scalar fields oscillate with different frequencies. Ref. [57] further considered a multi-state superposition. Ref. [16] studied the head-on collision of two spherical stars composed of different scalar fields. On the other hand, stationary solutions beyond spherical symmetry have also been obtained. Such is the case of the  $\ell$ -boson star [58] which considers a particular superposition of fields which preserves the spherical symmetry of the stress energy tensor; see [15] for a generalization that relaxes the constraint to obtain a family of solutions containing the  $\ell$ -boson star as well as the spinning and dipolar stars. The Newtonian version of this configuration was presented in Ref. [59], where the generalization goes one step further and considers more general/excited radial profiles with multiple nodes. The morphology of this last multi-state multipolar configuration has interesting cosmological applications [35, 42].

Q-balls [60, 61] (see [62] for a review) are the Minkowski space cousins of boson stars. Recently, it has been observed that for the model where spherical Q-balls exist, there also exist a tower of complex, multipolar Q-balls [63]. These “molecular states” of Q-balls, despite being metastable, can live for a long time [63–65], especially for the logarithmic potential [66]. These complex Q-balls have the intriguing feature that within a ball the co-existing positive and negative charges swap with time. The charge-swapping Q-balls are attractor solutions that can form from quite generic initial conditions [64, 66], and in particular they may form as a consequence of the Affleck-Dine(-like) condensate fragmentation in the early universe [66, 67], thanks to parametric resonance. On a slightly different note, it was recently observed that Q-balls and boson stars can induce superradiant amplification for scattering waves even in the spherically symmetrical cases [68–70].

In light of the similarity of Q-balls and boson stars, in this paper, we shall investigate the complex, charge-swapping structures of boson stars where both positive and negative charges co-exist within a star. We will explore the free scalar field case and the polynomial sextic and logarithmic scalar potentials, illustrating the key differences between potentials and uncovering situations where the gravitational interactions are essential for the existence of such configurations. We will construct complex boson stars by preparing the initial data with superpositions of spherical boson stars located close to each other, and letting the configuration evolve and relax to form multipolar boson stars. These charge-swapping multipolar boson stars are different from the static multipolar boson stars [55] mentioned above. First of all,

the charge-swapping boson stars are dynamical but with a well-defined morphology. However, the essential difference between the two is that: while in the static multipolar configurations the gravitational interaction is counteracted by a phase difference between the scalar field components, in the charge-swapping configurations it is the difference in the sign of the charge that allows the formation of the tower of multipolar configurations.

We also find that, while it is possible to achieve a considerable compactness, those charge-swapping boson stars in the large-size, low-compactness limit are well suited for a candidate for galactic dark matter halos. In such a scenario, the morphology of the dipolar configuration influences the structures moving in the outer region of the halo, and as a result, the galactic satellites moving around a host galaxy travel in coherently oriented planes. We shall explore the possibility of explaining the anisotropic distribution of satellite galaxies [71] by a charge-swapping dipolar galactic halo. These charge-swapping structures can be formed as a result of collisions of two structures with opposite charges, or, as mentioned, they can be formed by fragmentation of an Affleck-Dine-like condensate in the early universe.

This paper is organized as follows. In Section II we introduce the model, some relevant quantities used in the analysis and the explicit equations to treat charge-swapping boson stars as a Cauchy problem. After this, we also derive spherically symmetric boson stars and construct constraint-satisfying initial conditions after some clarification of the units and physical scales for our solutions. We then present and analyze the complex structures of boson stars for the minimally coupled free scalar theory in Section III and for self-interacting fields in Section IV. In Section V, we will discuss the possibility of using the dipolar charge-swapping configurations as a potential solution to the anisotropic distribution of satellite galaxies in the Milky Way. We conclude in Section VI.

*Conventions:* The metric signature is  $(-, +, +, +)$  and we choose the units with  $c = 1$ . Many dimensionful quantities are written with tildes, while the corresponding dimensionless quantities are without tildes.

## II. THEORY AND SETUP

We focus on a canonical  $U(1)$  symmetric scalar  $\Phi$  minimally coupled to gravity with action:

$$\tilde{S} = \int d^4\tilde{x} \sqrt{-g} \left( \frac{\tilde{R}}{16\pi G} + \mathcal{L}_\Phi \right), \quad (1)$$

where the Newton’s constant is  $G = 1/m_P^2$  and

$$\mathcal{L}_\Phi = -g^{\mu\nu} \frac{\partial\Phi^\dagger}{\partial\tilde{x}^\mu} \frac{\partial\Phi}{\partial\tilde{x}^\nu} - V(|\Phi|). \quad (2)$$

We will consider multiple choices for the potential  $V(|\Phi|)$  in this paper. We first consider the free, massive scalar

case in Section III

$$V(|\Phi|) = \mu^2 |\Phi|^2, \quad (3)$$

and in Section IV we add two different self-interactions to the scalar

$$V(|\Phi|) = \mu^2 |\Phi|^2 - \lambda |\Phi|^4 + \tilde{g} |\Phi|^6, \quad (4)$$

$$V(|\Phi|) = \mu^2 |\Phi|^2 \left( 1 + K \ln \frac{|\Phi|^2}{\mathcal{M}^2} \right). \quad (5)$$

The sextic potential can be considered as a leading truncation for the tree-level effective potential, and the high order terms are neglected as they are further suppressed as compared to the leading terms. The logarithmic interaction (5) is typical of quantum corrected effective potentials. As we see in Section IV B, the logarithmic potential is very similar to the free scalar case.

In the following of this section, we will use the sextic potential (4) as an example to set up the computational framework. (While the free field case is a special case of the sextic potential, we will comment on the differences for the logarithmic case.) It is useful to define the following dimensionless quantities

$$x^\mu = \mu \tilde{x}^\mu, \quad \phi = \frac{\sqrt{\lambda} \Phi}{\mu}, \quad \mathfrak{g} = \frac{\tilde{g} \mu^2}{\lambda^2}, \quad R = \frac{\tilde{R}}{\mu^2}, \quad (6)$$

similar to those used in [64]. With these dimensionless quantities, the action (1) with the sextic potential can be written as

$$S = \lambda \tilde{S} = \int d^4 x \sqrt{-g} \left( \frac{R}{16\pi\alpha_G} + \mathcal{L}_\phi \right), \quad (7)$$

where

$$\mathcal{L}_\phi = -g^{\mu\nu} \partial_\mu \phi^\dagger \partial_\nu \phi - V(|\phi|), \quad (8)$$

$$\text{with } V(|\phi|) = |\phi|^2 - |\phi|^4 + \mathfrak{g} |\phi|^6. \quad (9)$$

and we have defined an effective (dimensionless) gravitational constant

$$\alpha_G = \frac{G\mu^2}{\lambda} = \frac{\mu^2}{m_P^2 \lambda}, \quad (10)$$

which indicates the strength of the gravitational self-interaction in the presence of the self-interacting scalar field. That is, we can simply use action (7) to extract physics for the sextic potential with generic couplings  $\mu, \lambda, g$ , different choices of  $\mu$  and  $\lambda$  corresponding to scalings of the solution obtained with action (7). Of course, for the classical solution to be valid,  $\lambda$  should be relatively small, as its smallness can be linked to that of the reduced Planck constant:  $\tilde{S} = S/(\lambda\hbar)$ .

The free field potential (3) can be obtained from the sextic case by taking the limit  $\alpha_G \rightarrow \infty$  (and  $\tilde{g} \rightarrow 0$ ), where the  $|\phi|^4$  and  $\mathfrak{g}|\phi|^6$  terms become negligible, and the spherical solutions of the action (7) approach the mini-boson star sequence [1, 72]. In the opposite limit,

when  $\alpha_G \rightarrow 0$ , the gravitational backreaction vanishes, the spacetime reduces to Minkowski space and the stationary solutions become the Q-balls.

For the logarithmic potential, the corresponding quantities are defined as follows

$$x^\mu = \mu \tilde{x}^\mu, \quad \phi = \frac{\Phi}{\mathcal{M}}, \quad R = \frac{\tilde{R}}{\mu^2}, \quad (11)$$

Variation of the action (7) with respect to  $g_{\mu\nu}$  leads to the Einstein equations:

$$R_{\mu\nu} - \frac{1}{2} g_{\mu\nu} R = 8\pi\alpha_G T_{\mu\nu}, \quad (12a)$$

$$T_{\mu\nu} = g_{\mu\nu} \mathcal{L}_\phi - 2 \frac{\partial \mathcal{L}_\phi}{\partial g^{\mu\nu}}, \quad (12b)$$

and the  $\phi$  variation leads to the Klein-Gordon equation,

$$\nabla_\mu \nabla^\mu \phi = \frac{dV}{d(|\phi|^2)} \phi. \quad (13)$$

Now, we define some global quantities that will be useful in both the initial data construction and in the evolution of the dynamical system. The first one is the mass of a stationary spacetime. While in Minkowski space one can simply use the integral of the energy density  $T^{00}$

$$E = \int_{\Sigma_t} T^{00} \sqrt{\gamma} d^3 x. \quad (14)$$

as a measure of the total energy of the system, in curved spacetime other definitions need to be used to also account for the gravitational energy. We shall use the Komar integral associated to the Killing vector  $\xi = \partial_t$ ,

$$M_{\text{Komar}} = \frac{1}{4\pi\alpha_G} \int_{\Sigma_t} R_{\mu\nu} n^\mu \xi^\nu \sqrt{\gamma} d^3 x, \quad (15)$$

where  $\Sigma_t$  is a spacelike surface of constant  $t$  with  $n^\mu$  a vector normal to it and  $\gamma$  is the determinant of the spatial metric induced in  $\Sigma_t$ . We will further evaluate this integral in Section II A when we discuss the 3+1 decomposition of the equations of motion. The Komar mass reduces to  $E$  in Minkowski space for a stationary configuration. To see this, we use the Einstein equations, which gives

$$M_{\text{Komar}} = 2 \int_{\Sigma_t} \left( T_{\mu\nu} n^\mu \xi^\nu - \frac{1}{2} T n_\mu \xi^\mu \right) \sqrt{\gamma} d^3 x. \quad (16)$$

Then we use the fact that the integral over the  $T$  part of Eq. (16) vanishes due to the virial identity [73]. Strictly speaking,  $M_{\text{Komar}}$  is not a conserved quantity in non-stationary spacetimes. However, it remains useful, along with  $E$ , for approximately tracking the evolution of a gravitational system (see, e.g., [17, 18, 74]). Associated with the U(1) symmetry of the scalar field is the current

$$j_\kappa = i (\phi^\dagger \nabla_\kappa \phi - \phi \nabla_\kappa \phi^\dagger), \quad (17)$$

which is divergence-free and can be used to define a total scalar charge

$$Q = - \int n_\mu j^\mu \sqrt{\gamma} d^3 x. \quad (18)$$

### A. 3+1 decomposition

As we wish to study the complex, dynamical structures of boson stars, we will need to evolve the Einstein-Klein-Gordon system. This can be formulated as a Cauchy problem using a 3+1 decomposition

$$ds^2 = -\alpha^2 dt^2 + \gamma_{ij} (dx^i + \beta^i dt) (dx^j + \beta^j dt) . \quad (19)$$

Apart from the ‘‘coordinate’’-like variables  $\gamma_{ij}$ , the ‘‘velocity’’-like variables are given by the extrinsic curvature, defined by,

$$K_{ij} = -\frac{1}{2\alpha} (\partial_t - \mathcal{L}_\beta) \gamma_{ij} , \quad (20)$$

where  $\mathcal{L}$  denotes the Lie derivative. For the scalar field, we adopt the ‘‘velocity’’-like variable

$$K_\phi = -\frac{1}{2\alpha} (\partial_t - \mathcal{L}_\beta) \phi . \quad (21)$$

For a stable evolution of the gravitational system, we use the Baumgarte-Shapiro-Shibata-Nakamura-Oohara-Kojima (BSSNOK) formulation [75–77], which introduces auxiliary variables and makes use of a conformal metric with unit determinant  $\tilde{\gamma}_{ij} = \chi \gamma_{ij}$ . In this approach, one re-writes the equations of motion as follows (see, e.g., [78] for details),

$$(\partial_t - \mathcal{L}_\beta) \tilde{\gamma}_{ij} = -2\alpha \tilde{A}_{ij} , \quad (22a)$$

$$(\partial_t - \mathcal{L}_\beta) \chi = \frac{2}{3} \alpha \chi K , \quad (22b)$$

$$(\partial_t - \mathcal{L}_\beta) K = \chi \tilde{\gamma}^{ij} D_j D_i \alpha + \alpha \left( \tilde{A}_{ij} \tilde{A}^{ij} + \frac{1}{3} K^2 \right) + 4\pi \alpha_G \alpha (\rho + S) , \quad (22c)$$

$$(\partial_t - \mathcal{L}_\beta) \tilde{A}_{ij} = [\dots] - 8\pi \alpha_G \alpha \left( \chi S_{ij} - \frac{S}{3} \tilde{\gamma}_{ij} \right) , \quad (22d)$$

$$(\partial_t - \mathcal{L}_\beta) \tilde{\Gamma}^i = [\dots] - 16\pi \alpha_G \alpha \chi^{-1} P^i , \quad (22e)$$

$$(\partial_t - \mathcal{L}_\beta) \phi = -2\alpha K_\phi , \quad (22f)$$

$$(\partial_t - \mathcal{L}_\beta) K_\phi = \alpha \left[ K K_\phi - \frac{1}{2} \chi \tilde{\gamma}^{ij} \tilde{D}_i \partial_j \phi + \frac{1}{4} \tilde{\gamma}^{ij} \partial_i \phi \partial_j \chi + \frac{1}{2} (1 - 2|\phi|^2 + 3\mathfrak{g}|\phi|^4) \phi \right] - \frac{1}{2} \chi \tilde{\gamma}^{ij} \partial_i \alpha \partial_j \phi , \quad (22g)$$

where  $K$  is the trace of  $K_{ij}$ ,  $\tilde{A}_{ij}$  is the traceless part of the conformal extrinsic curvature,  $\tilde{D}_i$  ( $D_i$ ) is the covariant derivative compatible with  $\tilde{\gamma}_{ij}$  ( $\gamma_{ij}$ ),  $\tilde{\Gamma}^i$  are the conformal connection functions and we have defined the source terms

$$\begin{aligned} \rho &\equiv T^{\mu\nu} n_\mu n_\nu , & P_i &\equiv -\gamma_{i\mu} T^{\mu\nu} n_\nu , \\ S_{ij} &\equiv \gamma^\mu{}_i \gamma^\nu{}_j T_{\mu\nu} , & S &\equiv \gamma^{ij} S_{ij} . \end{aligned} \quad (23)$$

[...] in the equation for  $\tilde{A}_{ij}$  and  $\tilde{\Gamma}^i$  denote the standard quantities defined in the right-hand side of the BSSNOK equations, except for the source terms which have been

explicitly included above. The real and imaginary parts of the scalar field  $\phi$  are evolved separately in the actual code. Finally, the evolution is subject to a set of constraints given by

$$H \equiv {}^{(3)}R - K_{ij} K^{ij} + K^2 - 16\pi \alpha_G \rho = 0 , \quad (24)$$

$$\mathcal{M}_i \equiv D^j K_{ij} - D_i K - 8\pi \alpha_G P_i = 0 . \quad (25)$$

### B. Stationary isolated boson stars

We first consider an isolated, spherically symmetric boson star solution with a scalar field

$$\phi = f(r) \exp(-i\omega t) . \quad (26)$$

We choose the following ansatz for the spherical and static line element,

$$ds^2 = -\alpha^2(r) dt^2 + \Psi^4(r) (dr^2 + r^2 d\Omega^2) . \quad (27)$$

The solution for the functions  $f$ ,  $\alpha$ ,  $\Psi$  and the eigenvalue  $\omega$  can be obtained using the spectral code described in [79] to solve the following equations

$$\Delta_3 \Psi + 2\pi \alpha_G \Psi^5 \left[ \left( \frac{\omega f}{\alpha} \right)^2 + \frac{(\partial_r f)^2}{\Psi^4} + V_f \right] = 0 ,$$

$$\Delta_3 \alpha + \frac{2\partial_r \alpha \partial_r \Psi}{\Psi} - 8\pi \alpha_G \alpha \Psi^4 \left[ 2 \left( \frac{\omega f}{\alpha} \right)^2 - V_f \right] = 0 ,$$

$$\Delta_3 f + \frac{\partial_r f \partial_r \alpha}{\alpha} + 2 \frac{\partial_r f \partial_r \Psi}{\Psi} - \Psi^4 \left[ \frac{dV_f}{df^2} - \frac{\omega^2}{\alpha^2} \right] f = 0 , \quad (28)$$

where  $\Delta_3 := \partial_r^2 + \frac{2}{r} \partial_r$  and  $V_f = f^2 - f^4 + \mathfrak{g}f^6$ . This system of ordinary differential equations should be supplied with the boundary conditions from the regularity of the functions at  $r = 0$  and the asymptotic flatness of the spacetime:

$$\partial_r f|_{r=0} = \partial_r \alpha|_{r=0} = \partial_r \Psi|_{r=0} = 0 ; \quad (29)$$

$$f|_{r \rightarrow \infty} = 0 , \quad \alpha|_{r \rightarrow \infty} = \Psi|_{r \rightarrow \infty} = 1 . \quad (30)$$

Now let us obtain the specific expressions of the global quantities that will be used to characterize the stars. For an isolated boson star, it is easy to extract the ADM mass  $M_{\text{ADM}}$ , which can be read off from the asymptotic behavior of the metric functions far away from the center,  $\Psi^4 = 1 + 2\alpha_G M_{\text{ADM}}/r + \mathcal{O}(1/r^2)$ . Alternatively, we may evaluate the mass via the Komar integral (15), which for the spacetime (27) reduces to

$$M_{\text{Komar}} = \frac{1}{\alpha_G} \lim_{r \rightarrow \infty} \partial_r (r^2 \alpha) . \quad (31)$$

This coincides with  $M_{\text{ADM}}$  given that the spacetime is stationary [80]. In fact, we will use the relative difference between the masses as an error indicator for the spherical

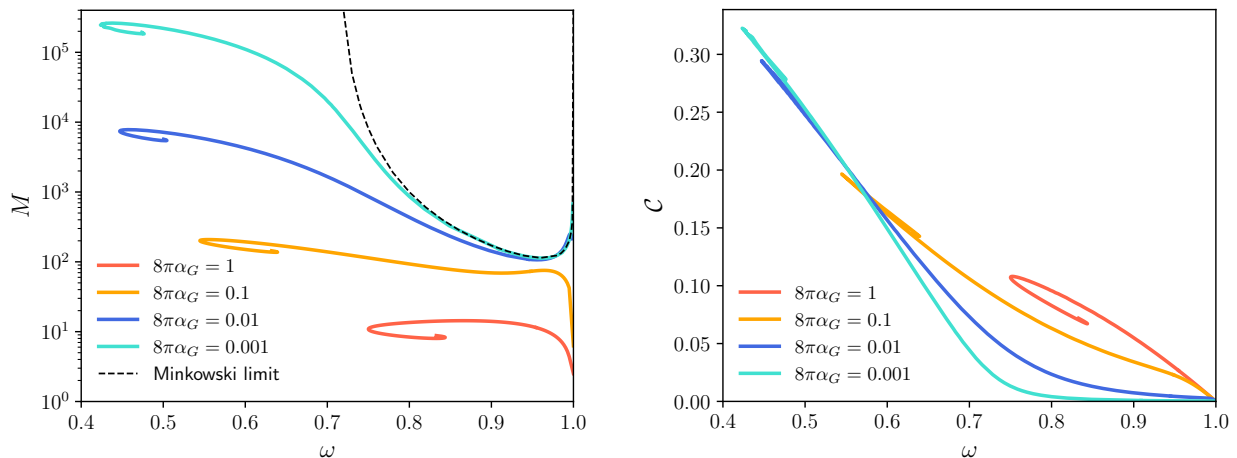


Figure 1. Dimensionless boson star mass  $M$  (left) and compactness  $\mathcal{C}$  (right) as a function of the frequency  $\omega$  for solutions with  $\mathfrak{g} = 1/2$  and different values of  $\alpha_G$ . We see that  $M$  converges to the Q-ball solution as  $\alpha_G \rightarrow 0$ . The extension of the stable branch for the cases with small (but not zero)  $\alpha_G$  is notable. Also note that the compactness for these configurations can span (even within the stable branch) from very small values up to high values, such as 0.3.

solver [30]. We will use  $M$  to refer to both masses in the following. For the U(1) charge of the scalar field, defined in Eq. (18), we get the following expression in the present case,

$$Q = 2 \int_{\Sigma_t} \frac{\omega f^2}{\alpha} \sqrt{\gamma} d^3x. \quad (32)$$

The radius  $R_{99}$ , commonly used to characterize the size of a boson star, refers to the value of areal radius that encompasses 99% of the total boson star mass. More specifically, this radius is defined in coordinates (27) as the value  $R_{99} = \Psi^2(r_{99})r_{99}$  such that the Misner-Sharp function  $M(r) = -2r/(1+r\partial_r \ln \Psi)$  evaluated at  $r = r_{99}$  is equal to  $0.99M$ . Finally, the compactness  $\mathcal{C}$  of a boson star will be defined as the mass  $M$  divided by  $R_{99}$

$$\mathcal{C} = \frac{M}{R_{99}}. \quad (33)$$

For every pair of  $(\alpha_G, \mathfrak{g})$ , there exists a family of solutions parametrized (in most cases) by the value of the scalar field at the center of the star,  $f_0$ . For  $\alpha_G \ll 1$ , we expect to recover the Q-ball solutions, and, in particular, the parameter space explored in [64]. In Fig. 1, we plot the mass and the compactness for sequences of solutions with different values of coupling constant  $\alpha_G$ . From the left panel of Fig. 1 we see that, contrary to what happens in the Q-ball case, the mass of the solutions is regularized at the maximal frequency  $\omega$ . Additionally, when gravity is introduced, solutions beyond the Q-ball thin-wall limit can exist. In our case, this limit is  $\omega = (1 - 1/(4\mathfrak{g}))^{1/2}$ . These solutions are of particular interest since, as can be seen in the right panel of Fig. 1, the compactness can reach very high values. For the corresponding static black hole, we have  $\mathcal{C} = 0.5$ , while the maximum of  $\mathcal{C}$  is around 0.1 for mini-boson stars ( $\lambda = 0 = \tilde{g}$ ) [81] and around 0.16

for strongly self-interacting boson stars (large  $\lambda/(G\mu^2)$ ,  $\tilde{g} = 0$ ) [2, 28].

In Fig. 2 we show a plot of the charge and energy-charge ratio for two families with  $\mathfrak{g} = 1/2$  and gravitational couplings  $\alpha_G = 1/(8\pi)$  and  $1/(8\pi \times 500)$ . From Fig. 1 we already see that the effect of gravity substantially modifies the configuration. In particular, when gravitational effects are strong (the top plot), the mass-charge ratio  $M/Q$  goes above 1 when  $\omega$  is close to the lower frequency limit. Note that  $M/Q \leq 1$  would be the stability condition of the Q-ball in the flat space limit, and for the Q-ball case,  $M/Q \leq 1$  is satisfied in the lower frequency limit, similar to the case of the bottom plot of Fig. 2. However,  $M/Q \leq 1$  may cease to be a reliable stability criterion in the presence of strong gravitational attractions. Nevertheless, the solution with a small value for  $\alpha_G$  approaches the Q-ball solution as expected, particularly in the region where the scalar field is smaller and hence the gravitational backreaction is weaker.

As mentioned in Section II, in the limit  $\alpha_G \rightarrow \infty$ , the model tends formally to the case of a free scalar field, which gives rise to mini-boson stars with the scalar field scaling inversely proportional to  $\sqrt{\alpha_G}$  when  $\alpha_G \gg 1$ . This tendency is consistent to what we see as we increase the value of  $\alpha_G$  in Fig. 1 and also Fig. 3 in the next section.

### C. Units and scales

In the above formulation, the mass  $M = M_{\text{ADM}} = M_{\text{Komar}}$  is dimensionless, so is the left part of the Einstein equations. To convert to the standard units, we can compare, for example, the asymptotic behavior of the metric in different units, from which we find  $\alpha_G M/r = G\tilde{M}/\tilde{r}$ , with  $\tilde{r}$  being the dimensionful radius. Therefore, we can

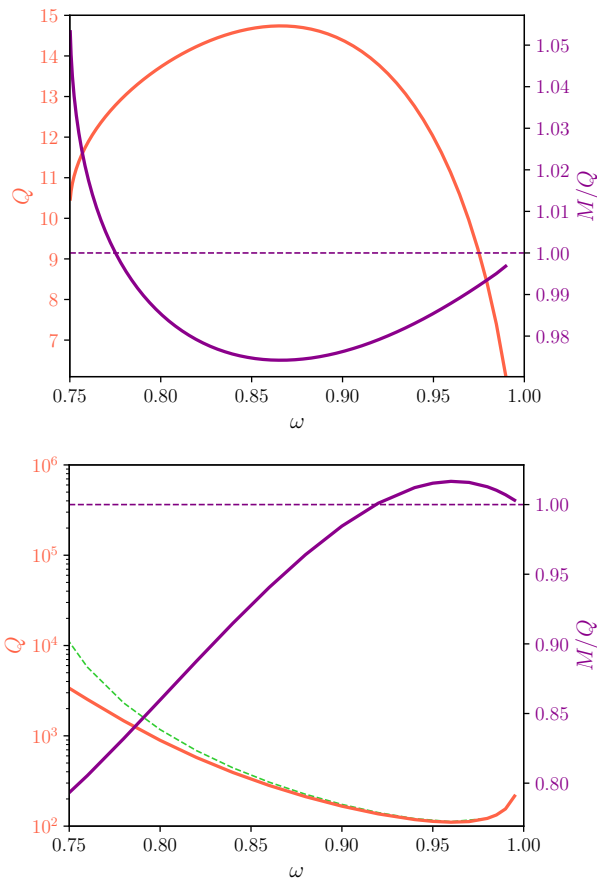


Figure 2. Sequence of isolated Q-stars with strong gravitational coupling  $8\pi\alpha_G = 1$  (top plot) and weak coupling  $8\pi\alpha_G = 0.002$  (bottom plot). The value of the Noether charge for the corresponding  $\alpha_G = 0$  (Q-ball) solution is also included as a green dotted line.

recover the standard units for the mass

$$\tilde{M} = \frac{\mu}{\lambda} M = \frac{\alpha_G}{G\mu} M. \quad (34)$$

In units of the solar mass, we have

$$\tilde{M} = (1.33 \times 10^{-10} \text{eV}/(\hbar\mu)) \alpha_G M M_\odot. \quad (35)$$

As one may expect, the Compton wavelength of the scalar  $\mu^{-1}$  more or less sets the typical length scale of the localized configurations. Given the scalar mass ( $\hbar\mu$ ), say, in electronvolts, then the length scale in kilometers or in parsecs is respectively given by

$$\mu^{-1} = \left( 1.97 \times 10^{-10} \frac{\text{eV}}{\hbar\mu} \right) \text{km} \quad (36)$$

$$= \left( 6.40 \times 10^{-24} \frac{\text{eV}}{\hbar\mu} \right) \text{pc}. \quad (37)$$

These numerical factors can be used quickly to convert to the standard units for any distance quantity  $\mu r$ . Both of them will be used in the following, km for astrophysical

applications and pc for the very dilute dark matter halo applications. See Fig. 3 for an example of this conversion.

Smaller values of  $\mu$  lead to configurations of the size of galactic dark matter halos. For example, this is the case for the ultralight cosmological scalar field [31, 32] with  $\hbar\mu \sim 10^{-22} \text{eV}$ , implying a Compton wavelength of  $\sim 0.1 \text{ pc}$  and sizes for the corresponding cold and dilute self-gravitating objects of  $\sim 1 \text{ kpc}$  [32]. We can also infer from Fig. 3 that in such cases, where an extremely low value of the compactness is expected, the present model with a variety of  $\alpha_G$ 's can give rise to solitonic solutions that fulfill that requirement.

From  $\alpha_G$ 's definition (10), we see that if the scalar coupling  $\hbar\lambda$  is around  $\mathcal{O}(0.1)$ , then  $\alpha_G$  is an extremely small number if  $\mu^{-1}$  is of the kilometer scale, since  $m_P \sim 10^{19} \text{ GeV}$ . These cases essentially reduce to Q-balls, which for a kilometer scale  $\mu^{-1}$  is astronomical in size. A larger  $\alpha_G$  is obtained if either  $\mu$  is close to the Planck mass or  $\lambda$  is highly suppressed, say, around  $\hbar\lambda \sim \mathcal{O}(10^{-10})$ . For the former case, since  $\mu$  sets the size of the localized configuration, these objects are quite small. The later corresponds to astronomical structures such as stars or larger objects.

#### D. Preparing complex boson stars: solving initial constraints

General Relativity is highly nonlinear, and the gravitational field in general does not obey a linear superposition law. Thus, we can not simply superpose boson star solutions, which is in general not a solution, and let it relax toward a complex boson star configuration. We need to carefully prepare the initial data by solving the Hamiltonian and momentum constraints. The 3+1 formalism with a scalar field as a source was presented in Section II A. For our purposes, we shall choose  $K_{ij} = 0$  at  $t = 0$ , which means that the momentum density  $P^i$  of the initial data that we intend to construct vanishes, that is, we wish to start with two clumps standing initially with zero velocity. The extrinsic curvature vanishes for time symmetric data, and therefore we can ignore the momentum constraints (25) and solve only the Hamiltonian constraint (24), which in this case is reduced to

$$H \equiv {}^{(3)}R - 16\pi\alpha_G\rho = 0. \quad (38)$$

We shall solve the Hamiltonian constraint by an iterative method. To that end, we start from the scalar configuration  $f^{(\text{BS})}$  of a spherical boson star. With the  $f^{(\text{BS})}$  configuration, as an initial guess, we can prepare, for example, the dipolar scalar configuration by placing a boson star and an anti-boson star on the  $z$ -axis separated by distance  $d$ ,

$$\phi = f^{(\text{BS})}(x, y, z - d/2)e^{-i\omega t} + f^{(\text{BS})}(x, y, z + d/2)e^{i\omega t}. \quad (39)$$

Similarly, for the canonical momentum of the scalar field,

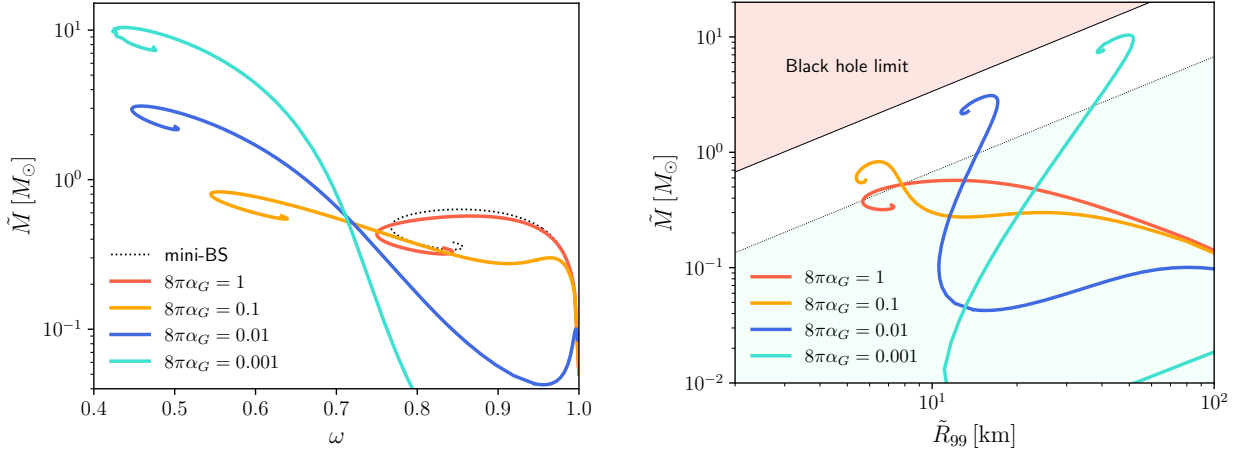


Figure 3. Sequence of solutions with  $\mathfrak{g} = 1/2$  and for scalar mass  $\hbar\mu = 1.33 \times 10^{-10}$  eV. In the right plot, we indicate with a red band the region with compactness above the black hole limit  $\mathcal{C} = 1/2$ . The big light blue band corresponds to the compactness bound of mini-boson stars. The models with smaller values of  $\alpha_G$  can reach higher values of compactness. The masses of most of the stable configurations in this example are of the order of the solar mass, while their radii are as small as tens of kilometers. For reference, the radius of the Sun is  $R_\odot = 7 \times 10^5$  km. We can also see from both panels of this figure that the solutions approach the mini-boson star case as  $\alpha_G$  increases.

we use the initial input

$$K_\phi = K_\phi^{(\text{BS})}(x, y, z - d/2) + K_\phi^{(\text{aBS})}(x, y, z + d/2). \quad (40)$$

where  $K_\phi^{(\text{BS})} = i\omega f^{(\text{BS})} e^{-i\omega t} / (2\alpha^{(\text{BS})})$  and  $K_\phi^{(\text{aBS})} = -i\omega f^{(\text{BS})} e^{i\omega t} / (2\alpha^{(\text{BS})})$ . Then, we make a simple superposition of the corresponding gravitational fields. This setup gives us the initial guess in the Newton iterative scheme used to solve the Hamiltonian constraint. In the following we explain the procedure we follow to choose the initial guess for the spacetime metric and then obtain a solution to the Hamiltonian constraint.

We shall choose to solve Eq. (38) using the conformal thin-sandwich approach, where the 3+1 spatial metric is related to the conformal metric  $\bar{\gamma}_{ij}$  by  $\gamma_{ij} = \psi^4 \bar{\gamma}_{ij}$ . Now, according to Eq. (27), the spatial metric of an isolated boson star in these coordinates is simply  $\gamma_{ij}^{(\text{BS})} = \Psi_{(\text{BS})}^4 \delta_{ij}$ . Recall that the background metrics for an isolated boson star and anti-boson star are the same, so we choose the conformal metric  $\bar{\gamma}_{ij}$  to be a simple superposition of the spatial metric [18, 20],

$$\bar{\gamma}_{ij}(\mathbf{r}) = A(\mathbf{r})^2 \delta_{ij} \quad (41)$$

where we define the function  $A$  in spherical coordinates<sup>1</sup>

<sup>1</sup> Although in the dipolar case both  $\phi$  and  $K_\phi$  depend only on  $r$  and  $\theta$ , we here also keep track of the  $\varphi$  angle dependence in the geometric and scalar field quantities so that the generalization to the multipolar case is straightforward to obtain from the equations presented here. For the dipole solutions, both the simple superposition guess  $\bar{\gamma}_{ij}$  and the expected solution  $\gamma_{ij}$  for the Hamiltonian constraint are axisymmetric, so we also have  $A = A(r, \theta)$ .

as

$$A(r, \theta, \varphi) = \left( \Psi_{(\text{BS})}^4(x, y, z - d/2) + \Psi_{(\text{BS})}^4(x, y, z + d/2) - 1 \right)^{1/2}. \quad (42)$$

The full spatial line element in spherical coordinates reads

$$dl^2 = \psi^4(r, \theta, \varphi) A^2(r, \theta, \varphi) (dr^2 + r^2 d\Omega^2). \quad (43)$$

In the conformal thin-sandwich formulation, the Hamiltonian constraint becomes the Lichnerowicz equation

$$\tilde{D}^2 \psi - 1/8 \psi^{(3)} \tilde{R} = -2\pi \psi^5 \rho, \quad (44)$$

where  $\tilde{D}$  is the covariant derivative associated with  $\bar{\gamma}$  and  $^{(3)}\tilde{R}$  is the 3-dimensional Ricci scalar of  $\bar{\gamma}_{ij}$ . For the initial guess for the conformal factor, we choose  $\psi(r, \theta, \varphi) = 1$ , because of the conformal metric we have chosen. Furthermore, we take as initial data for the lapse function  $\alpha$  a simple superposition [16, 19, 21, 74]  $\alpha(r, \theta) = \alpha^{(\text{BS})}(x, y, z - d/2) + \alpha^{(\text{BS})}(x, y, z + d/2) - 1$ . See Refs. [18, 20, 82, 83] for other possibilities.

In order to solve the Hamiltonian constraint we calculate

$$^{(3)}\tilde{R} = -\frac{2}{A^3} \left( 2\Delta_3 A - \frac{\partial A \partial A}{A} \right), \quad (45)$$

and

$$\tilde{D}^2 \psi = \frac{1}{A^2} \Delta_3 \psi + \frac{1}{A^3} \partial A \partial \psi, \quad (46)$$

where we have used the 3-dimensional Laplacian and the scalar product of the gradients in spherical coordinates

$$\Delta_3 = \partial_r^2 + \frac{2\partial_r}{r} + \frac{\partial_\theta^2}{r^2} + \frac{\partial_\theta}{r^2 \tan \theta} + \frac{\partial_\varphi^2}{r^2 \sin^2 \theta}, \quad (47)$$

$$\partial u \partial v = \partial_r u \partial_r v + \frac{\partial_\theta u \partial_\theta v}{r^2} + \frac{\partial_\varphi u \partial_\varphi v}{r^2 \sin^2 \theta}. \quad (48)$$

For the dipolar configuration, when applied to the fields  $A$  and  $\psi$ , the derivatives with respect to  $\varphi$  do not contribute. All that remains is to obtain the energy density, which can be calculated from Eq. (23) using the metric of the spatial slice, leading to

$$\rho = 4K_\phi K_\phi^\dagger + \frac{\partial\phi\partial\phi^\dagger}{\psi^4 A^2} + |\phi|^2 - |\phi|^4 + \mathfrak{g}|\phi|^6. \quad (49)$$

It is important to note that  $\rho$  depends on  $\psi$ , so it must be updated at each iteration in the root-finding procedure used by the elliptic solver for the Hamiltonian constraint. This approach differs from the one typically employed in the context of fluid stars, where energy and momentum are fixed quantities, allowing for straightforward reconstruction of fluid variables. In our case, if  $\rho$  is fixed, the scalar field variables can only be reconstructed after solving the Hamiltonian, which involves finding the scalar field that corresponds to the given  $\rho$  through a differential equation. This process is complex and can result in initial data that do not accurately represent the physical situation of interest. Specifically, in charge-swapping configurations, we fix the scalar field initial data (39), (40) and treat them as the essential quantities we can control to achieve the desired dynamical configurations. As a consequence,  $\rho$  becomes a derived quantity, which can lead to issues of non-uniqueness in the solutions of Eq. (44).

A comprehensive discussion of this issue in the context of initial data construction for boson stars can be found in Ref.[82]. In our implementation, we do not encounter alternative solutions and conduct three tests to assess the robustness of the code. First, we observe that the solutions for isolated boson stars ( $\psi = 1$ ) act as local attractors in the solution space, given the method used to solve the Lichnerowicz equation (44). Second, we find that as the stars are moved farther apart, the solution converges to the  $\psi = 1$  case as the distance  $d$  increases. Finally, we experiment with different implementations using superpositions other than those in Eq.(42), yet the (physical) metric coefficient  $\psi^4 A^2$  consistently converges to the same solution.

In the following we describe in more detail how we solve the Lichnerowicz equation (44) in practice. Combining Eqs. (45), (46) and (49), we arrive at the following partial differential equation:

$$\Delta_3 \psi + \frac{\partial A \partial \psi}{A} + \frac{\psi}{4} \left( \frac{2\Delta_3 A}{A} - \frac{\partial A \partial A}{A^2} \right) + 2\pi\alpha_G \psi^5 A^2 \rho = 0, \quad (50)$$

which needs to be solved with the following boundary conditions:

$$\psi_{r \rightarrow \infty} = 1, \quad \partial_r \psi|_{r=0} = 0, \quad \partial_\theta \psi|_{\theta=0, \pi} = 0. \quad (51)$$

We solve this elliptic partial differential equation using the `Kadath` library [84, 85]. This spectral solver has been utilized in various theoretical physics scenarios, particularly for constructing axisymmetric boson stars [30, 33]. Besides the axisymmetric dipolar case, we will also be interested in solving Eq. (50) without axisymmetry for the quadrupole and octupole cases. To this end, we employ the *spherical space* facility implemented in the library, which uses spherical coordinates and decomposes the space into spherical shells with the possibility of placing as the last shell one with a compactified radial coordinate such that boundary conditions at infinity can be imposed exactly. Full details of this space can be found Ref. [85] where the `Kadath` solver was presented.

In the spherical space of the library, the spectral basis functions used in the decomposition of the fields are chosen such that regularity at the origin is ensured and the parity of the fields with respect to  $\theta = \pi/2$  plane is respected. In essence, the spectral code will deal with the spectral coefficients  $F_{ijk}$  of certain function  $F$ . If the function is unknown, the code will try to find the solution through a Newton-Raphson iterative scheme once an initial guess for  $F_{ijk}$  or equivalently  $F$  is given. For our case, the unknown function is the conformal factor. Roughly speaking, the fields are decomposed into Chebyshev polynomials in the radial domain. In the  $\theta$  domain, sines and cosines of definite parity are used, and for the  $\varphi$  angle, a simple Fourier decomposition is utilized. The particular relation between  $F$  and  $F_{ijk}$  is,

$$F(r, \theta, \varphi) = \sum_{i=0}^{N_r} \sum_{j=0}^{N_\theta} \left[ \sum_{k=0, k \text{ even}}^{N_\varphi} F_{ijk} \cos(m\varphi) + \sum_{k=1, k \text{ odd}}^{N_\varphi} F_{ijk} \sin(m\varphi) \right] \Theta_j(\theta) X_i(x) \quad (52)$$

with  $m = \lfloor k/2 \rfloor$  and  $x$  is some function that maps  $r$  to the domain  $[-1, 1]$ , which depends on the particular radial domain considered. In the inner domain, the (basis) functions  $X_i$  and  $\Theta_j$  are defined according to the oddness of the integer  $m$  and the symmetry of the function  $F$  with respect to the  $\theta = \pi/2$  plane. For  $F$  symmetric,

$$X_i = T_{2i}(x), \Theta_j = \cos(2j\theta) \quad \text{if } m \text{ is even,}$$

$$X_i = T_{2j+1}(x), \Theta_j = \sin((2j+1)\theta) \quad \text{if } m \text{ is odd.}$$

For  $F$  antisymmetric,

$$X_i = T_{2i+1}(x), \Theta_j = \cos((2j+1)\theta) \quad \text{if } m \text{ is even,}$$

$$X_i = T_{2j}(x), \Theta_j = \sin((2j)\theta) \quad \text{if } m \text{ is odd.}$$

For the outer domain, the basis functions are simply chosen as  $X_i(x) = T_i(x)$  independently of the properties of  $m$  and  $F$ .

The concrete form of the decomposition of the odd and even functions is then used to transfer the initial data from the coefficient space (3D array provided by `Kadath`) to a 3D `Einstein Toolkit` mesh. For instance, in the case of the dipole, the function  $\phi$  and the metric coefficients are symmetric functions with respect to the equatorial plane, but  $K_\phi$  is anti-symmetric.

### III. FREE SCALAR

We shall first consider complex boson stars that are charge-swapping in the model where the scalar potential is simply

$$V(|\phi|) = |\phi|^2. \quad (53)$$

This can be formally obtained by taking the limit  $\alpha_G \rightarrow \infty$  and  $\mathfrak{g}/\alpha_G^2 \rightarrow 0$  from the sextic potential. The gravitational attraction makes it possible to have charge-swapping solitons even for this quadratic/free potential. In this model, stable (mini-)boson stars exist from the zero mass limit,  $\omega = 1$ , up to the critical mass [22] located at  $\omega = 0.853$  and<sup>2</sup>  $\alpha_G M = 0.633$ ; see Fig. 3. This stability range of boson stars restricts the domain of configurations we can use to prepare “molecular states” of boson stars.

At first glance, one might expect that only by superposing configurations such that the total mass does not significantly exceed the critical value of an isolated boson star can such charge-swapping configurations be formed. However, on the initial relaxation stage, the system can radiate away a significant amount of the initial energy, and therefore the charge-swapping configuration can emerge from a large initial mass. Nevertheless, it is also true that if the initial mass exceeds a critical value, the final state typically is a black hole. Considering this, we choose six cases of mini-boson stars with frequencies between 0.95 and 0.995. The information about these isolated boson stars is summarized in Table I.

To determine how the system evolves, the initial data are exported into the evolution scheme Eqs. (22), implemented in the open source `Einstein Toolkit` infrastructure [86, 87] using the `McLachan` [88] thorn to evolve the metric quantities and a modified version of the `Scalar` thorn [23, 89] to evolve the scalar field. To track the formation of apparent horizons we use the `AHFinderDirect` [90]. The evolution is implemented with a grid spacing of  $\Delta x^i = 1.6$  and a Courant factor of  $\Delta t/\Delta x = 0.125$

and with different fixed refinement levels included in the `Carpet` thorn [91]. In all cases, the size of the computational domain box is at least twice that of  $d + 2R_{99}$  (the approximate size of the configuration at  $t = 0$ ) for the configuration with the highest compactness and largest  $d$ .

The particular size of the domain and the distribution of the refinement level will be specified in the following and kept fixed for all the simulations in the same section for an easy comparison. As discussed in [64] and [66], boundary conditions are important when investigating the lifetime of a charge-swapping configuration. In line with this, we have also employed absorbing (radiative) boundary conditions that are usual for boson star simulations. For the scalar field, we use the standard Sommerfield boundary conditions but additionally include the first order correction to the massless scalar field dispersion relation [9]:  $\partial_t K_\phi = -\partial_r K_\phi - K_\phi/r + \mu^2 \alpha \phi/4$  at  $r \rightarrow \infty$ . As for the gauge freedoms, we impose the “Gamma-driver” condition [92] for the shift vector  $\beta^i$  and the “1+log” condition [93] for the lapse  $\alpha$ .

The interpolation from the initial data spectral coefficients and the analysis of various quantities during the evolution are done using separate thorns also within the `Cactus` framework. The choices of the numerical setup employed in this work have been tested in the Appendix.

#### A. Dipolar (charge-swapping) boson star

For the dipolar boson star, we initially prepare a superposition of two spherical boson stars with opposite charges but the same values of  $|\omega|$ , which take the first four rows of Table I, corresponding to  $\omega = 0.95, 0.96, 0.97$  and  $0.98$ . Then, following the procedure presented in Section II D, there is only one more parameter to choose: the initial distance between the superposed stars  $d$ . We vary  $d$  between 0 and 36 in steps of 6 for the four fre-

$\omega$	$\alpha_G M$	$\alpha_G Q$	$R_{99}$	$\mathcal{C}$	$\alpha_G E$	$\sim d_{\min}$
0.95	0.490	0.497	17.4	0.0296	0.388	> 36
0.96	0.450	0.455	18.9	0.0235	0.373	36
0.97	0.399	0.403	21.7	0.0186	0.347	24
0.98	0.334	0.336	27.3	0.0123	0.304	18
0.99	0.242	0.243	40.6	0.0058	0.231	-
0.995	0.173	0.174	55.4	0.0032	0.171	-

Table I. Classical observables of the mini-boson stars used in the preparation of charge-swapping boson stars. All of them correspond to low-compactness stars. The value of  $E$  is calculated using the integral (14), despite that it only characterizes the total energy of the solution in the weak-field limit. The value  $d_{\min}$  in the last column corresponds to the minimal distance between the centers of the boson stars in the dipolar case such that a long-living boson-anti boson star configuration can form. The configurations with “-” in the last column, represent cases not explored or discussed in the dipolar scenario.

<sup>2</sup> In the limit  $\alpha_G \rightarrow \infty$  the dimensionless mass  $M$ , energy  $E$  and other quantities scale as  $\alpha_G^{-1}$ , so we include  $\alpha_G$  factors to make them finite. However, it is important to say that after restoring units with the formulas given in Section II, the physical mass and Noether charge of the solutions in the  $\alpha_G \rightarrow \infty$  limit correspond to the expected mini-boson star finite quantities (as they should). For instance for the critical mass  $\bar{M} = 0.633/(G\mu)$ , as expected for the Kaup limit solution.

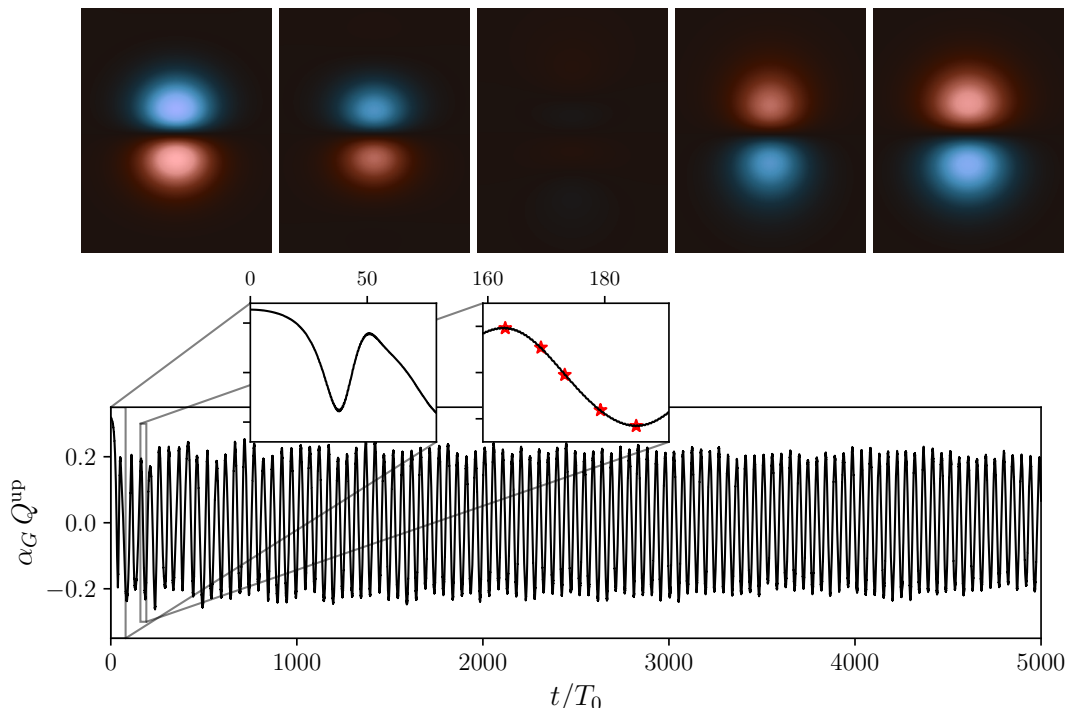


Figure 4. Evolution of charge density  $-n_\mu j^\mu$  in a half charge-swapping period plotted in the  $xz$  plane for a dipole configuration (top panel). The color scheme uses blue for positive charge, red for negative charge and black for zero charge, with the numerical values ranging  $\pm 3.6 \times 10^{-4}$ . We also show the evolution of the total Noether charge in the  $z > 0$  half space,  $Q^{\text{up}}$ , for the configuration initially constructed by superposing two boson stars with  $\omega = \pm 0.98$  and separated by  $d = 24$  initially (bottom panel). The inset in the left shows the initial relaxation process. The points in the inset of the right show the five snapshots of the top panel.  $T_0 = 2\pi$  is the characteristic time of the scalar field and also roughly the oscillation frequency of the two initial constituent stars. However, the charge-swapping frequency is much larger. The height of the boxes in the top panel snapshots is  $\Delta z = 28$ . The inset can be seen in even greater detail in Fig. 5. In accordance with footnote 2 we use  $\alpha_G$  to reconstruct the finite and physical quantity associated to the Noether charge.

quencies. For the low compactness case with  $\omega = 0.98$ , which is our fiducial model, we also explore  $d = 42$ . This gives a total of 25 simulations for the free-field dipole case, for which we choose a cubic grid of side 160 and use the mirror-symmetry in the plane  $xz$  and  $yz$  to reduce the computational cost by a factor of 4. We use three refinement levels with a grid-spacing of  $\Delta x = 0.4$  in the finest grid, refining the grid in each level by a factor of two.

We find that if the initial distance is too small, or the solution too compact, an apparent horizon is formed and the scalar field configuration results in gravitational collapse within  $t \sim 10^3$ . For a fixed value of  $\omega$ , we observe that as the distance  $d$  increases, a greater amount of energy is radiated away in the initial relaxation period. Nevertheless, if the stars in Table I are placed sufficiently far away from each other initially, they can attract and relax to form a charge-swapping configuration.

A typical scenario of a charge-swapping boson star forming is shown in Fig. 4. The first observation is that, unlike their flat spacetime counterparts with a polynomial potential [64], there is no indication of decay or a subsequent final oscillation stage with total  $Q = 0$ . For

all configurations where a charge-swapping boson star successfully forms in the free field case, the evolution exhibits only two qualitatively distinct stages: an initial relaxation phase, followed by a charge-swapping plateau.

The first stage is depicted in the left inset of Fig. 4. In this specific case, we consider initial boson stars with a radius of  $R_{99} = 27.3$ , initially separated by a distance of  $d = 24$ . Consistent with these parameters, the charge swap begins promptly after  $t = 0$ , indicating that the initial configuration is relatively close to the charge-swapping bound state. We observe that the U(1) charge in the  $z > 0$  half-space,  $Q^{\text{up}}$ , starts oscillating with an amplitude slightly smaller than the initial one. This reduction is due to a small portion of the scalar field being ejected shortly after the simulation begins. Although, in this example, the stars are already very close to each other at  $t = 0$ , it is important to say, as we will discuss later, that in some cases, positioning the stars farther apart is crucial for achieving a charge-swapping pattern. In these cases we will refer to the early part of the initial relaxation stage, when the stars meet and start interacting both gravitationally and through scalar field interactions leading to the interchange of Noether charge, as the

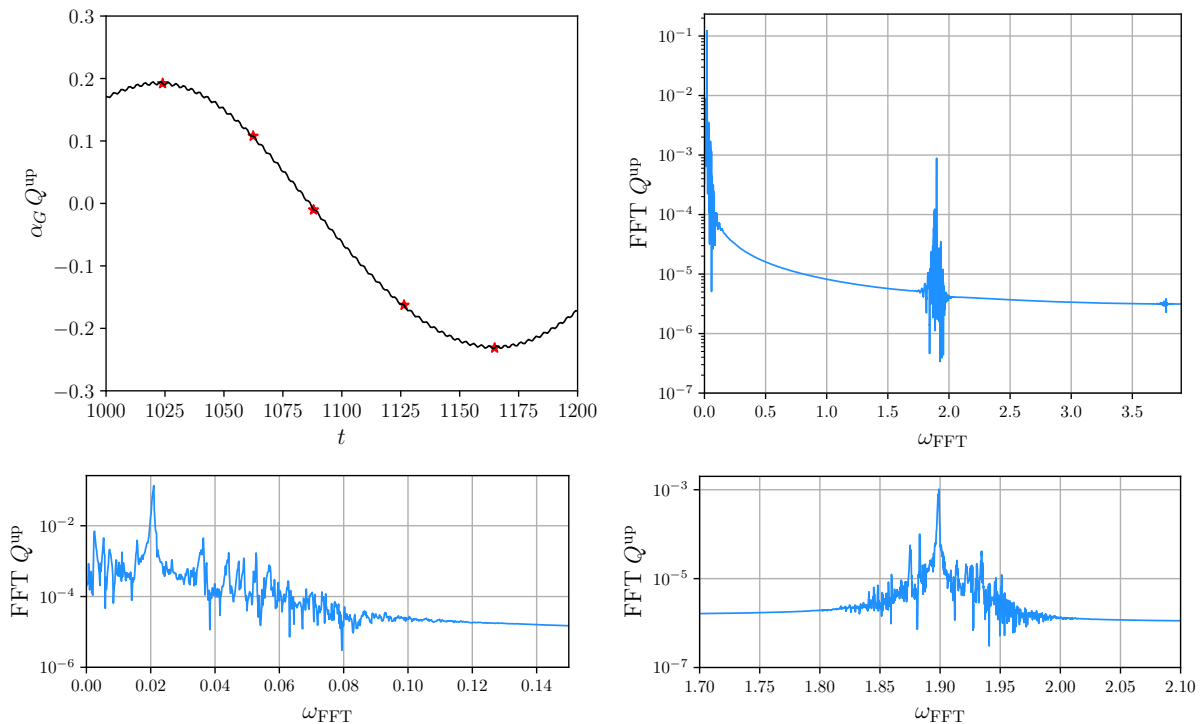


Figure 5. Amplification of the inset in Fig. 4 (top left panel) and Fourier transform of  $Q^{\text{up}}$  for the temporal waveform in Fig. 4. The two main peak regions are amplified in the bottom panels.

merger phase.

In the top panel of Fig. 4, we show half of a charge-swapping period, with the first plot and the last plot showing that the positive and negative charges have been completely inverted during this half period.

For  $\omega = 0.98$ , we find that below the value  $d = 24$ , which is the one showed in Fig. 4, the next case, which is  $d = 18$ , also forms a regular horizonless final configuration, but the configuration with  $d = 12$  forms a black hole. So according to the mapping of the parameter space we use, the minimum distance to form a boson-anti boson regular system is  $d_{\text{min}} = 18$ . For  $\omega = 0.97$ , which is both more massive and compact, we find a bigger minimum distance  $d_{\text{min}} = 24$  is required. The trend continues with the 0.96 and 0.95 cases as displayed in the last column of Table I. Of course, the configurations with smaller  $\omega$  are initially smaller and, as they require a larger initial distance to avoid collapse, the merger of the stars is delayed. For these cases, and before the merger, the charge  $Q^{\text{up}}$  remains constant, then decreases (at the merger) and starts to oscillate regularly once the initial relaxation period (which can be violent) is over. The process is similar to what we will show to happen in the quadrupolar case in Fig. 9 below.

The charge-swapping configuration analyzed in Fig. 4 and all the other charge-swapping configurations we surveyed have very long lifetimes. Given that  $T_0 = 2\pi$  is approximately the oscillation period of the scalar field, we find that the complex boson star survives for at least

5000  $T_0$ . For a selection of these simulations, we have let them evolve for three times as long, and we find that they continue oscillating without decay.

The charge distribution of the formed configurations contains some strong Fourier modes which are visible immediately if we combine Fig. 4 together with the first panel in Fig. 5. As was explicitly demonstrated already in Ref. [64] for the Q-ball case, the most important frequency is related to the global difference between the real and the imaginary part of the scalar field. In the boson star case, this is induced not by a nonlinear scalar potential, but by the gravitational effects. In Fig. 5, we also show the temporal Fourier transforms of  $Q^{\text{up}}$  (top right panel), for the waveform presented in Fig. 4. We also see from the bottom panels of Fig. 5 that the period of charge swapping is around  $T_{\text{swap}} = 2 \times 150$ , since the dominant peak is around  $\omega_{\text{FFT}} = 0.02 \approx 2\pi/300$ . The other low frequency modes, which modulate the amplitude of  $Q^{\text{up}}$ , are present to the left of this dominant peak (see the bottom left panel of Fig. 5). Similar to the flat space-time charge-swapping solutions [63, 64], we see a high frequency oscillation which corresponds to the small undulations visible in the top left panel of Fig. 5, having a peak frequency close to  $\omega_{\text{FFT}} = 1.9$  (see the bottom right panel).

One can verify that the difference between the frequencies of the real and imaginary component of the scalar field is the origin of the dominant oscillation mode of the charge distribution. To see this, we make a spec-

tral decomposition of the scalar field at a point outside the origin—at the origin, the imaginary part of  $\phi$  is zero by construction. We see from Fig. 6 that the scalar field is practically monochromatic and the difference between the maximum of the real and imaginary parts gives  $\omega_R - \omega_I = 0.020$  (see the caption of Fig. 6 for more details), which is consistent with the dominant peak of  $Q^{\text{up}}$ . In addition, we also find a second peak which is located around the first odd multiple of the base frequency, analogously to what was found in [64] and consistent with the fact that a scalar potential has a  $\mathbb{Z}_2$  symmetry. On the other hand, the small oscillations of  $Q^{\text{up}}$  that we already discussed corresponding the peak in the bottom right panel of Fig. 5, coincide very well with  $\omega_R + \omega_I = 1.898$  and can be shown to be produced by the next order perturbation term on the charge density  $\propto j^0$ , after the term with frequency  $\omega_R - \omega_I$ .

The other free-field dipolar solutions also have a clear harmonic dependence in time, so we have extracted the averaged period of  $\phi$  for these cases and displayed the information in Table II. We see that for a given value of the (initial) frequency  $\omega$ , the angular frequency of the scalar field in the formed configuration increases with  $d$  (more energy is radiated away during the initial relaxation phase) and the configuration evolves to a “more Newtonian” configuration. Also, notice that the angular frequency is always smaller than the corresponding value at  $t = 0$ ,  $\omega$ . This is actually opposite to the behavior of single unstable boson star undergoing gravitational cooling [11] and tending to a stable configuration.

In addition to tracking the evolution of  $Q^{\text{up}}$ , we utilize the integral described in Eq. (14) to monitor the evolution of the systems. We find that the integral  $E$ , plotted in Fig. 7, converges gradually to a nonzero value (at least for the time probed by our simulations). Specifically, for a fixed  $\omega$ ,  $E$  decreases as  $d$  increases.

$\omega$	$d$	period	afreq.
0.98	18	6.783	0.926
0.98	24	6.697	0.938
0.98	30	6.642	0.946
0.98	36	6.609	0.951
0.98	42	6.588	0.954
0.97	24	6.942	0.905
0.97	30	6.858	0.916
0.97	36	6.810	0.932
0.96	36	7.132	0.881

Table II. Averaged period for  $\Re \phi(0, 0, 0)$  for several free-field cases, considering various different initial separations. We only list the simulations where a charge-swapping configuration is formed. The period is defined as the time elapsed between two zero points of  $\phi(0, 0, 0)$  where  $\partial_t \phi(0, 0, 0) > 0$ , averaged over the data from  $t = 10^2 T_0$  to  $t = 5 \times 10^3 T_0$ . The angular frequency (afreq.) refers to  $2\pi$  divided by this averaged period.

## B. Higher multipolar boson stars

Dipolar boson stars formed after a head-on collision of two boson stars were previously observed and shown to survive at least until  $t \sim 200 T_0$  [21]. In the previous subsection, we observed that these objects can actually exist for much longer periods and display an intriguing charge-swapping pattern. However, to the best of our knowledge, no tower of composite stars with multipolar distribution has been reported. In the case of Q-balls, these configurations do exist [63], and we now examine whether it is possible to generalize the dipolar case to get configurations formed of positive and negative charge pairs with more general morphologies. To this end, in this subsection, we consider superpositions of four as well as eight stars with equal and opposite charges, and place them in quadrupole and octupole configurations respectively.

In Section IID, we have used the dipolar case as an example to illustrate the preparation of the initial data for the simulations. In particular, we specified how to solve the Hamiltonian constraint. For the quadrupolar case, the procedure is similar. Now, we can place spherical stars centered at the vertices of a square with side length  $d$  and positioned in the  $xz$  plane:

$$\begin{aligned} \phi = & f^{(\text{BS})}(x - d/2, y, z - d/2)e^{-i\omega t} \\ & + f^{(\text{BS})}(x - d/2, y, z + d/2)e^{i\omega t} \\ & + f^{(\text{BS})}(x + d/2, y, z - d/2)e^{i\omega t} \\ & + f^{(\text{BS})}(x + d/2, y, z + d/2)e^{-i\omega t}. \end{aligned} \quad (54)$$

Consequently, for the canonical momentum, we impose

$$\begin{aligned} K_\phi = & K_\phi^{(\text{BS})}(x - d/2, y, z - d/2) \\ & + K_\phi^{(\text{aBS})}(x - d/2, y, z + d/2) \\ & + K_\phi^{(\text{aBS})}(x + d/2, y, z - d/2) \\ & + K_\phi^{(\text{BS})}(x + d/2, y, z + d/2). \end{aligned} \quad (55)$$

After this, the generalization for the superposition of the conformal metric and the lapse function is straightforward. The rest of the procedure is exactly the same, since we have formulated the equations between Eq. (43) and Eq. (50) without assuming any particular symmetry.

The orientation of the square defined by the centers of the stars at  $t = 0$ , as given by Eq. (54), is selected to minimize adjustments in the implementation within Kadath, particularly concerning the parity of the fields used in the solution. However, to make better use of the Einstein Toolkit resources, we choose to perform a transformation of the coordinates  $x^i = \Lambda^i_j x'^j$  with  $\Lambda$  being the rotation matrix around the  $y$ -axis  $R_y(\delta)$ ,  $\delta$  being the rotation angle. Taking  $\delta = \pi/4$ , the system has mirror-symmetry<sup>3</sup> with respect to the three  $x^i = 0$  planes and

<sup>3</sup> In the thorn arrangement used for the simulations, only mirror-

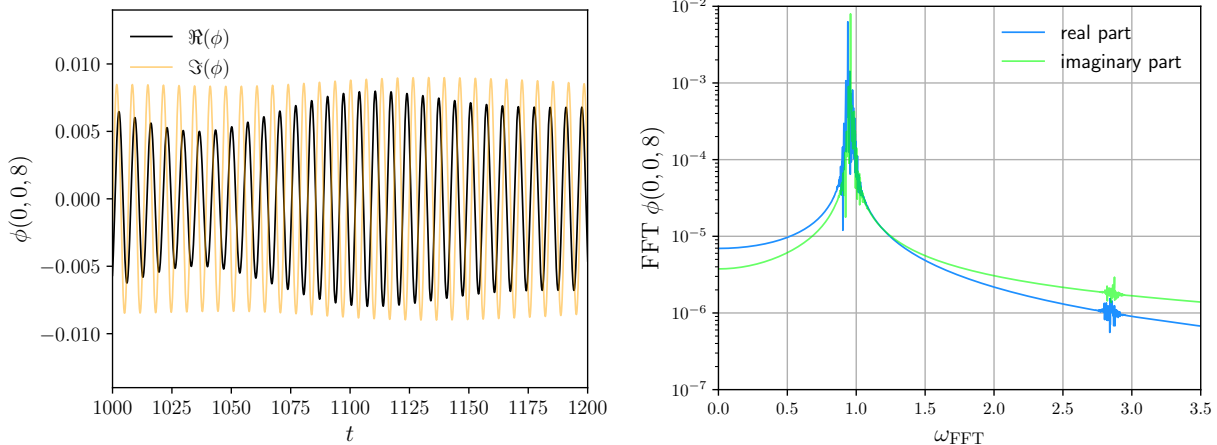


Figure 6. Real and imaginary part of the scalar field in the same time window as the half-period inset of Fig. 4 and evaluated at  $(x, y, z) = (0, 0, 8)$  (left panel). The right panel is the Fourier decomposition of the scalar field, the blue line corresponding to the (fast) Fourier transform of the real part, while the green one to the imaginary part. The maxima are at  $\omega_r = 0.939$  and  $\omega_i = 0.959$  respectively. The phase difference between  $\Re(\phi)$  and  $\Im(\phi)$  is changed in this time window between  $t = 1000$  and  $t = 1200$ .

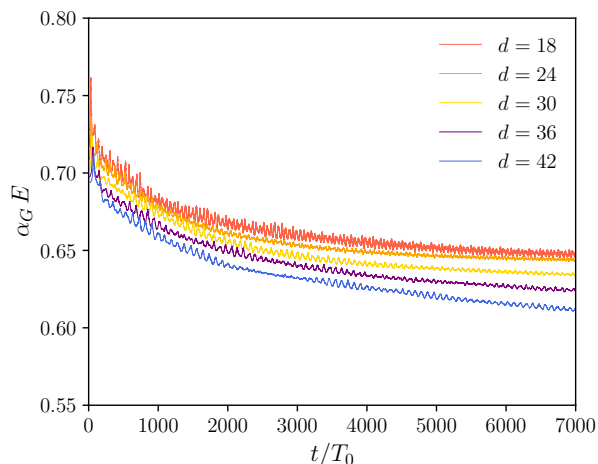


Figure 7. Energy functional defined in Eq. (14) for several free scalar field dipoles using different initial distances for configurations prepared with  $\omega = 0.98$ .

the computational cost is reduced by a factor of eight. So this is actually faster than the dipole case. Nevertheless, the quadrupolar configurations are larger in size. Thus, for these simulations, we double the mesh size and the refinement level boundaries.

We find that none of the first five types of spherical stars in Table I leads to charge-swapping configurations for the same range of  $d$  as in the dipole case, not even extending up to a value of  $d = 48$ . Black holes are of-

ten formed instead. In contrast, the last two types of stars with frequencies of 0.99 and 0.995 are capable of forming non-trivial configurations that are everywhere regular. Stationary boson stars with these frequencies are very dilute, as can be seen from their values of  $\mathcal{C}$  and radius  $R_{99}$  in Table I. We have tried three  $d$  distances for these two  $\omega$ 's respectively: 48, 42 and 36, and find that for both  $\omega$ 's no apparent horizon is formed for  $d = 42$  and 48, but for  $d = 36$  (and also smaller values), the initial clump collapses to a black hole. In Fig. 8, we can see the collapse of the lapse for one of the quadrupole cases together with the corresponding dipolar case which does not collapse.

Configurations that avoid collapse exhibit quadrupolar charge-swapping structures. Despite differing shapes, these structures show quantitative similarities to the dipolar case, following similar correlations between initial parameters  $\omega$  and  $d$ , and the final solution properties. However, their lifetimes differ markedly from self-interacting quadrupoles without gravity (*i.e.*, quadrupolar Q-balls) [64], with all cases persisting for at least  $t = 5000T_0$ . In Fig. 9, snapshots of charge density illustrate typical behavior, comparing initial star distributions at  $t = 0$  with those within half a charge-swapping period later in the simulation. The bottom panel of Fig. 9 shows  $Q^{\text{quad}}$ , the total charge associated with one blob by integrating  $n_\mu j^\mu$  over the  $z > |x|$  region.

In this case, compared to the analogous plot for a dipole shown in Fig. 4, the initial relaxation process begins later. Specifically, because the four stars are initially far apart, the Noether charge  $Q^{\text{quad}}$  remains positive until approximately  $t/T_0 \sim 50$ , when the merger occurs. Following the merger, relaxation begins, and regular stable oscillations of the charge are observed after  $t/T_0 \sim 100$ . We have found that the scalar field ejected

---

symmetry itself can be imposed on the scalar field, but not the anti-symmetry.

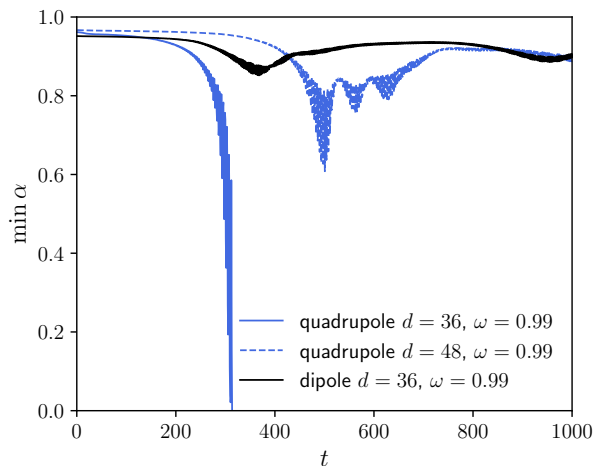


Figure 8. Minimum value of the lapse function for two free field quadrupole cases with  $\omega = 0.99$  and two different values of  $d$ . For comparison, we add the curve of the  $\min \alpha$  for the dipolar case with the same values of  $d$  and  $\omega$  as the collapsing configuration.

at the merger of dipolar and quadrupolar cases is essential to obtain a charge-swapping configuration.

It is natural to ask whether there are higher order multipolar boson stars. So far, all our preliminary attempts to use the method described in Section II D to find solutions have resulted in the configurations collapsing into black holes. As there is more mass involved in a small space, one can try to increase the distance  $d$ , but that leads to a decrease of the gravitational attraction. However, it is possible that octupolar boson stars may be constructed with a more systematical parameter scan or an improved preparation method.

#### IV. SELF-INTERACTING SCALAR

Now, we include self-interactions for the U(1) scalar. In the flat space, they provide attractions for non-topological solitons and their molecular states to form. In the presence of gravity, scalar self-interactions can increase the compactness and the masses of boson stars. We will consider two types of interactions: a polynomial potential truncated to the sixth order and a soft logarithmic correction to the mass term, the charge-swapping Q-balls of which have been previously studied [63, 64, 66].

##### A. Sextic potential

The boson stars in the sextic potential model

$$V(|\phi|) = |\phi|^2 - |\phi|^4 + \mathbf{g}|\phi|^6 \quad (56)$$

exist within the range  $\omega_{\min} < \omega < 1$  with  $\omega_{\min}$  some value that depends on  $\alpha_G$  and  $\mathbf{g}$  (see Fig. 1 for a sextic

$\alpha_G (\times 8\pi)$	$\omega$	$M$	$Q$	$R_{99}$	$C$	$E$
0.001	0.8	863.5	1009	8.40	0.00407	843.9
0.01	0.8	433.6	491.8	7.40	0.0235	375.4
0.01	0.75	865.7	1052	8.02	0.0417	678.7
0.01	0.7	1660	2152	9.03	0.0728	1113
0.1	0.7	138.8	159.1	5.22	0.1050	67.42

Table III. Global quantities of the boson stars used in the preparation of self-interacting charge-swapping configurations. All of them correspond to the model with  $\mathbf{g} = 1/2$ . Notice that all of them correspond to low compactness stars.  $E$  is calculated using the integral in Eq. (14) which tends to  $M$  as  $\alpha_G$  takes smaller values, consistent with the discussion below Eq. (16).

family of solutions with fixed  $\mathbf{g}$  and different  $\alpha_G$ ). As already discussed, gravity regularizes the total energy of the solutions in the limit  $\omega \rightarrow 1$ . In fact,  $M \rightarrow 0$  at such limit for all cases (except  $\alpha_G = 0$ ). This is often known as the Newtonian limit.

According to our numerical experiments, starting from the Newtonian limit and increasing the value of  $f(r=0)$ , there exist stable solutions whenever

$$\frac{dM}{d\omega} < 0 \quad (57)$$

until the turning point  $\omega_{\min}$ . This leads to one or two stable branches according to the value of  $\alpha_G$ ; see Fig. 1. These observations are consistent with the conclusions drawn from a stability analysis of such solutions using catastrophe theory [24, 25]. After the turning point, all solutions are unstable regardless of the sign of  $dM/d\omega$ , some of them migrating toward a stable boson star and others dissipating to infinity or collapsing to a black hole depending on the binding energy, which is similar to the free field and the quartic self-interaction cases previously reported in the literature [9, 10].

Compared to the free field case, the self-interacting solutions are qualitatively very different when the gravitational coupling is small, where they are close to their Q-ball counterparts. Nevertheless, these cases can give rise to very compact solutions (as  $f(r=0)$  increases) that differ significantly from the Q-ball solutions and achieve very high compactness, making them different from both the mini-boson stars and the corresponding Q-balls; see Fig. 3. With this in mind, we have chosen the stars in Table III to prepare the charge-swapping configurations. In particular, we restrict our study to superpositions of single star solutions that are stable on their own. Of course, this does not guarantee that the complex boson star solution will be obtained, and neither ensures that the final solution will not be a black hole. Since we have fixed  $\mathbf{g} = 1/2$  as our fiducial model, we only have two degrees of freedom to construct the initial data:  $\omega$  and  $d$ .

We shall explore the dipole superposition with initial separations  $d = \{8, 10, 12, 14, 16\}$ . Before proceeding with the boson star analysis, as a sanity check, we

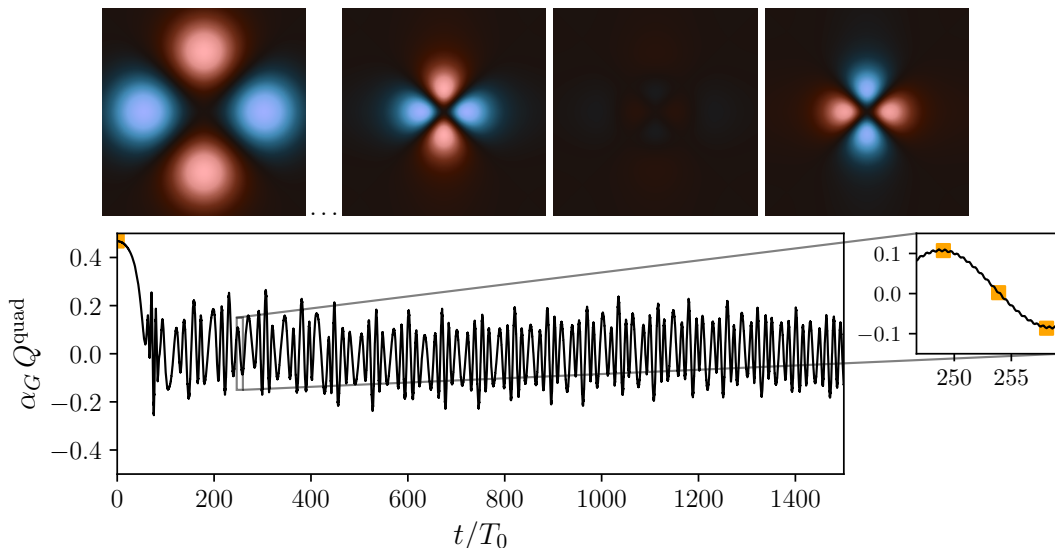


Figure 9. Charge density at  $t = 0$  of four boson stars with  $\omega = 0.99$  and located at the vertices of a square with side length  $d = 42$  (top left panel) and three snapshots within half a charge-swapping period when the quadrupolar charge-swapping configuration has formed (top right panel). The 2D plots of the top panels correspond to the  $xz$  plane. The color scheme uses blue for a positive density, red for a negative one and black for zero. The range of values spans from  $-5.3 \times 10^{-5}$  to  $5.3 \times 10^{-5}$ . The box size is 50 for the top left panel, and 16 for the top right three boxes. We also show that the integral of the charge density over  $z > |x|$ ,  $Q^{\text{quad}}$ , as a function of  $t$  (bottom panel). The points in the inset show the four snapshots of the top panels.

first re-produce the 3+1D results of charge-swapping Q-balls in Ref. [64], The resulting flat spacetime evolutions are shown in Fig. 10. We will see that the charge-swapping configurations, when gravity is included, share many properties with the flat spacetime limit analogue. In this sense the Fig. 10 is representative of some of the properties that are obtained in general. There are four stages present when charge-swapping configurations are successfully obtained: An initial relaxation stage, which ends around  $t = 500T_0$  for the case presented in Fig. 10; a plateau stage of charge-swapping, ending around  $t = 1000T_0$ ; a fast decay stage in which  $Q^{\text{up}}$  drops abruptly to zero and the energy density also decreases but towards a finite spherically symmetric state; a long-lived stage of the (highly perturbed) oscillaton [94], the oscillon in the absence of gravity (see Ref. [95] for related real vector field solitons with cosmological applications).

Unlike the analysis conducted for the free field case, in all the scenarios explored with the sextic potential, we positioned the stars initially close together. For instance, in all the figures presented in this section, the maximum distance  $d$  considered is 16. When comparing this to the radii of the stars listed in Table III, it is evident that the stars are either “touching” or very close to each other initially in nearly all cases. Typically, the repulsive self-interaction from the quartic term is sufficient to prevent gravitational collapse, making the consideration of larger initial separations less relevant for the sextic potential compared to the free field scalar case. Consequently, the early stages of the relaxation process, including the merger, occur rapidly after the initial con-

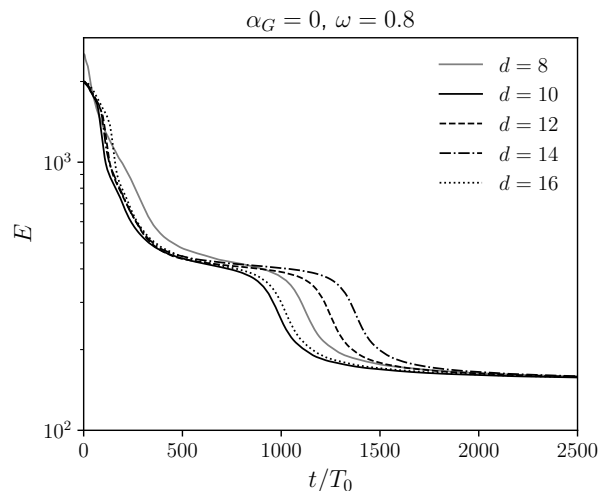


Figure 10. Flat spacetime simulations for the sextic model with  $\mathfrak{g} = 1/2$ . We plot the energy as a function of time varying  $d$  for fixed  $\omega = 0.8$ . The  $d = 14$  case is consistent with that of Ref. [64].

figuration of the stars.

We see from Fig. 10 that the longest lifetime is given by  $\omega = 0.8$  and  $d = 14$ , consistent with that of Ref. [64], among other results. These flat-space solutions have smaller radii than the free-field configurations with gravity discussed in Section III. Nevertheless, for an easy comparison, we keep the same numerical setting as in the dipolar free field case with gravity.

Next, we switch on  $\alpha_G$  to investigate the effect of introducing the gravitational interaction. To monitor the evolution in this case, although not perfect as it is now not really conserved, we will still use the  $E$  integral as a proxy. In all the cases presented in this section, we observe that the envelope of the Noether charge in the upper hemisphere always follows a similar qualitative behavior to that of the  $E(t)$  curve. In Fig. 11, we show the cases with frequency  $\omega = 0.8$  and gravitational coupling  $8\pi\alpha_G = 0.001$  and  $0.01$ . This corresponds to the two first rows in Table III. For  $8\pi\alpha_G = 0.001$ ,  $\omega = 0.8$  is the point where the spherical boson stars start to deviate from the Q-ball counterparts (see Fig. 1). The same is also noticeable in the top panel of Fig. 11 for the charge-swapping configurations, where we see that the lifetimes are slightly shortened in the presence of gravity for all the  $d$ 's listed. For a smaller  $\alpha_G$ , the system basically reduces to the Q-ball case. For  $8\pi\alpha_G = 0.01$  in the bottom panel, interestingly, we see that the differences between the  $E$  curves are negligible for different  $d$ 's, due to the significantly reduced lifetimes. This means that the gravitational interaction is already dominating for  $8\pi\alpha_G = 0.01$ , and the stable end state corresponds to an oscillaton as expected. To confirm that the final stage is indeed an oscillaton, we examine the quantity  $Q^{\text{up}}$ . In regions where this quantity approaches zero, we analyze the phase portraits of the complex scalar field, specifically plotting  $\Re(\phi)$  versus  $\Im(\phi)$ . During the oscillaton stage, the phase portraits exhibit oscillations along a single linear direction.

In these cases presented in Fig. 11, as well as in the  $\alpha_G \rightarrow 0$  limit another relevant mechanism takes place in the formation of charge-swapping states. When self-interaction is significant this mechanism is characterized by a net attraction force arising from the nonlinear scalar field, which is specific to charge-swapping systems and has been detailed in Ref. [63] for Q-balls. In our configurations, when the quartic term of the scalar potential is large and the effective gravitational constant is therefore small, this property predominates in the attraction between the two blobs, facilitating the formation of bound states. In the free-field scenario, this effect is absent, with the gravitational interaction being the sole force that holds the stars together. As we will demonstrate, when we increase the value of  $\alpha_G$  for the sextic potential case under examination in this section, the interaction that initially facilitated the formation of bound states becomes subdominant, allowing gravity to dominate the dynamics of the system.

Now, we turn to the cases where the initial boson stars are not similar to the Q-ball analogue with the same value of  $\omega$ . This corresponds to the three last rows in Table III. The two configurations with  $\omega = 0.7$  are beyond the so-called thin-wall limit of the corresponding Q-ball model, and in particular the star with  $8\pi\alpha_G = 0.1$  has a larger compactness than any of the stable mini-boson stars,  $\max \mathcal{C}_{\text{mini}} = 0.08$  [28]. We find that the charge-swapping configurations can be created for the cases with  $8\pi\alpha_G = 0.01$  and  $\omega = 0.7$  or  $0.75$ , but they collapse in

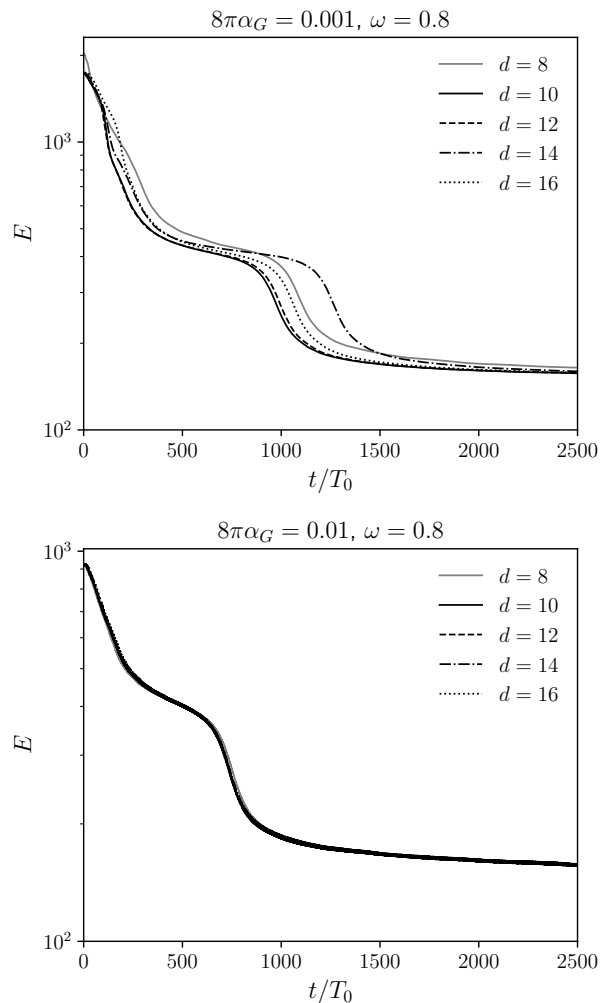


Figure 11. Almost the same setup as Fig. 10 but with the gravitational coupling  $\alpha_G$  switched on. Again we vary  $d$  and  $\alpha_G$  for fixed  $\omega = 0.8$ .

the  $8\pi\alpha_G = 0.1$  case.

The evolution of  $E$  for  $\omega = 0.75$  and  $8\pi\alpha_G = 0.01$  for three different  $d$ 's together with the total Noether charge in the  $z > 0$  region for  $d = 16$  is shown in Fig. 12. We can see how the charge is radiated away in the final stage. More interesting is the fact that for these cases, as well as for the cases in Fig. 13, the configuration transits through two charge-swapping plateaus with different  $E$  and  $Q^{\text{up}}$  before migrating to the oscillaton configuration. This resembles the cascading of the energy for excited oscillons [96]. However, at the level of the quantities we have observed, a direct connection between the two phenomena has yet to be established.

The case beyond the thin-wall limit with  $8\pi\alpha_G = 0.01$  is shown in Fig. 13. For  $8\pi\alpha_G = 0.1$ , similar setups would lead to gravitational collapse, without stabilizing first to a finite value of  $E$  or  $Q^{\text{up}}$ .

The last comment we shall make for the case of the sextic potential is that isolated boson stars differ from

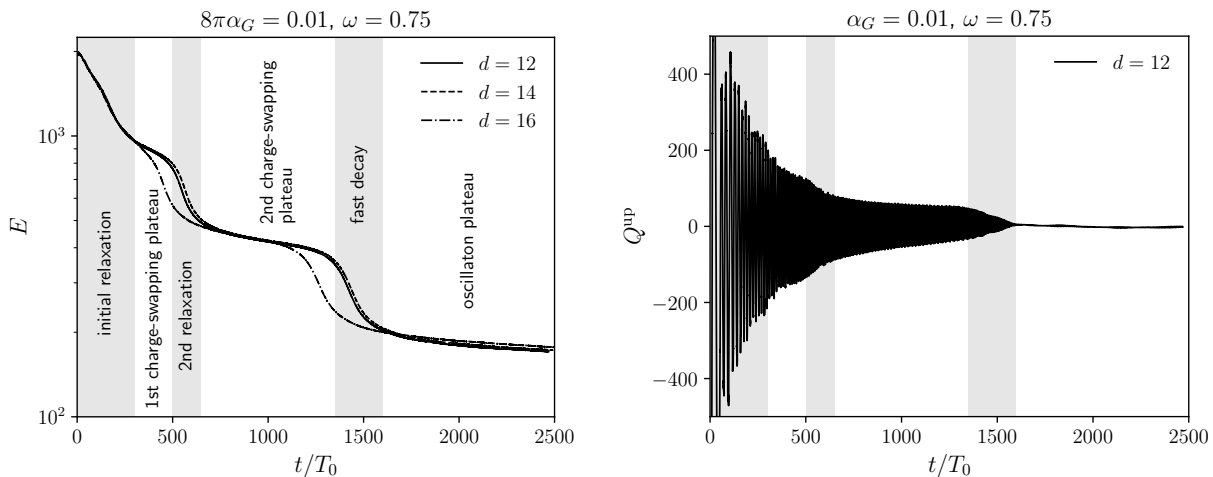


Figure 12. Varying  $d$  for fixed  $\omega = 0.75$ . In the right panel we show the Noether charge in the  $z > 0$  region,  $Q^{\text{up}}$ , only for the  $d = 12$  case. For reference we mark the different stages of the evolution for this case in both plots.

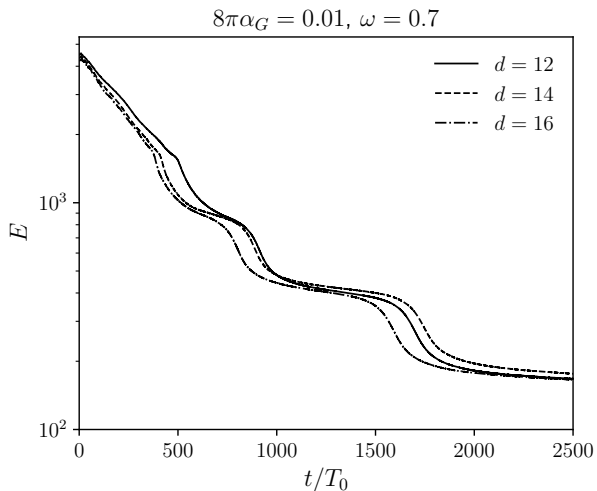


Figure 13. Varying  $d$  for fixed  $\omega = 0.7$  and  $8\pi\alpha_G = 0.01$ . This self-gravitating configuration was prepared using boson stars with initial frequencies smaller than those allowed by the flat spacetime Q-ball thin-wall limit.

Q-balls not only in cases near or beyond the thin-wall limit but also in the region where gravity regularizes the solutions near  $\omega = 1$ . Since in this limit the total mass of the solution tends to zero, the curve of  $M$  vs  $\omega$  (or radius) is “forced” to form a stable Newtonian solution branch. In this branch, the stationary solutions of the sextic potential converge to those of the quadratic potential in the limit, due to the fact that  $\phi \rightarrow 0$  in this limit; see [46] for a systematical study of several kinds of self-interactions. It is therefore expected that configurations prepared using this branch of solutions will lead to the same results as those presented in Section III.

## B. Logarithmic potential

Polynomial potentials naturally arise as effective potentials when integrating out weakly coupled heavy degrees of freedom. On the other hand, when including quantum corrections, the potential often picks up some logarithmic dependence. These potentials are widely studied for the case of Q-balls [97–102], and capable of creating very long-lived charge-swapping Q-balls [63, 66]. In this subsection, we consider a complex scalar field minimally coupled with Einstein gravity with a potential of the kind,

$$V(|\Phi|) = \mu^2 |\Phi|^2 \left( 1 + K \ln \frac{|\Phi|^2}{\mathcal{M}^2} \right), \quad (58)$$

where  $K$  is a negative coefficient that we will fix to  $K = -0.1$  in the following and the parameters  $M$  and  $\mu$  are scales that can be absorbed by redefinitions.

As mentioned previously, it is also possible to obtain a dimensionless action in terms of dimensionless variables and parameters. To this end, we simply choose  $x^\mu = \mu \tilde{x}^\mu$  and  $\phi = \Phi/\mathcal{M}$ . In doing so, we again gain control over the gravitational interaction, defining in this case  $\alpha_G = \mathcal{M}^2 G$  while rescaling the Ricci scalar as in the sextic potential case. Thus, we can study the action  $\tilde{S} = \mathcal{M}^2 S/\mu^2$  instead, with the dimensionless potential given by

$$V(|\phi|) = |\phi|^2 (1 + K \ln |\phi|^2). \quad (59)$$

Once again the equations of motion for the gravitational and scalar fields are given by Eqs. (12) and (13).

An interesting property of this model is that in the Minkowski limit ( $\alpha_G \rightarrow 0$ ), the equation of motion for  $\phi$

$$-\frac{\partial^2 \phi}{\partial t^2} + \Delta_3 \phi = [1 + K(1 + \ln |\phi|^2)] \phi, \quad (60)$$

admits an exact spherical solution

$$\phi = \exp\left(\frac{\omega^2 - 1}{2K} + 1\right) \exp\left(\frac{Kr^2}{2}\right) \exp(-i\omega t). \quad (61)$$

Then, in order to build complex boson star solutions, we take this as initial guess and slowly increase the value of  $\alpha_G$ , solving once again for the function  $f$  of the ansatz  $\phi = f(r)e^{-i\omega t}$  and the metric coefficients  $\alpha$  and  $\Psi$  using Eqs. (28) with the logarithmic potential. Then we proceed to prepare initial data for charge-swapping configurations following the same procedure as described in Section IID. The opposite limit  $\alpha_G \rightarrow \infty$  needs to be considered with more care, but is beyond the scope of this work.

Sequences of the spherical boson stars for the logarithmic potential are presented in Fig. 14 for five different values of the gravitational coupling constant. In this figure, we have included also the  $\alpha_G \rightarrow 0$  limit, which can be obtained by substituting Eq. (61) into Eqs. (14) and (18), giving rise to the following expressions for  $E = M$  and  $Q$ ,

$$M = \left(-\frac{\pi}{K}\right)^{3/2} (2\omega^2 - K) \exp\left[\frac{\omega^2 - 1}{K} + 2\right], \quad (62)$$

$$Q = 2 \left(-\frac{\pi}{K}\right)^{3/2} \omega \exp\left[\frac{\omega^2 - 1}{K} + 2\right]. \quad (63)$$

For all the boson star families plotted in Fig. 14, we find that, interestingly, the frequency  $\omega$  of the critical mass increases with  $\alpha_G$ . To the best of our knowledge, no such boson stars have been previously constructed in the literature (see [34] where a different logarithmic potential was explored). Consequently, no results are available on the stability of such spherical boson stars. We can anticipate that beyond the critical mass point the configuration is unstable, as is the case for most (if not all) families of spherical boson stars available in the literature. On the other hand, configurations to the right of the respective maxima in Fig. 14 are potentially stable, so we use spherical boson stars with  $\omega = 1.2$  to prepare charge-swapping configurations. In Table IV, we display the classical observables of the logarithmic boson star solutions we will use.

Interestingly, all the presumably stable configurations shown in Table IV have a positive binding energy

$$E_{\text{bind}} = M - Q. \quad (64)$$

This is different to all the other cases explored in this work, Tables I and III. This can be seen from the exact expression for  $M$  and  $Q$  (see Eqs. (62) and (63)). Yet, these configurations survive even against finite perturbations for a very long time. We have explored the 5 configurations in the Table IV together with the fiducial model in [66] and have not seen any of these configurations decay within our simulation limits. Thus, they are perfectly suitable for preparing charge-swapping configurations.

$\alpha_G (\times 8\pi)$	$M$	$Q$	$R_{99}$	$\mathcal{C}$	$E$
0.0001	47.54	38.29	7.76	$2.4 \times 10^{-5}$	46.78
0.001	46.97	37.82	7.71	$2.4 \times 10^{-4}$	46.15
0.01	42.15	33.88	7.68	$2.2 \times 10^{-3}$	40.85
0.1	22.98	18.29	7.22	0.0127	20.66
1	5.512	4.287	6.38	0.0343	4.176

Table IV. Mass, charge, radius and other global properties of the boson stars used in the preparation of logarithmic charge-swapping configurations. All of them correspond to the model with  $K = -0.1$  and have a frequency  $\omega = 1.2$ . This corresponds to the gravitational generalization of the fiducial model explored in [66]. The value of  $E$  is calculated using the integral in Eq. (14), which tends to the value of  $M$  when  $\alpha_G$  is small.

We take a dipole superposition with  $d = 2$  for the five cases in Table IV, and evolve them using a modified scalar field thorn in a mesh with the same specifications as those of the sextic potential case. The configurations are of the same size. We find that all of them form long-lived charge-swapping configurations except for the case with  $8\pi\alpha_G = 1$ , which promptly collapses to a black hole before any charge-swapping takes place. All the other cases are very long-lived and survive at least until  $t = 60000$ .

As in the sextic potential case, here we also prepared configurations that are close to each other at  $t = 0$ , so in this sense we are expected to start with states close to the charge-swapping configuration. Interestingly, similar to the charge-swapping Q-ball case with the logarithmic potential, there is no relaxation process that radiates away excess of the scalar field, as can be confirmed in Fig. 15. Also, the charge-swapping process begins very early in the simulations. The latter is reflected in the fact that the charge-swapping period  $T_{\text{swap}}$  is clearly defined from the beginning of the evolution, as can be seen in Fig. 16:  $T_{\text{swap}}$  is defined as twice the time elapsed between two contiguous zero points of the Noether charge in the upper half space  $Q^{\text{up}}$ .

## V. ANISOTROPIC DISTRIBUTION OF SATELLITE GALAXIES

In the last two sections, we have explored generic features of complex boson stars, particularly their lifetimes and the charge distributions. As we have seen, these “molecular states” of boson stars are often quite stable and with distinct charge-swapping patterns. The sizes of these objects are not explicitly specified in these simulations, and in fact,  $\mu^{-1}$  is essentially used as a base length, setting their characteristic sizes. In this section, we shall discuss one specific application of these objects in galactic scales.

For the lowest order/dipolar charge-swapping configuration, its energy density distribution is almost constant with time, mostly spherical but distorted with an appre-

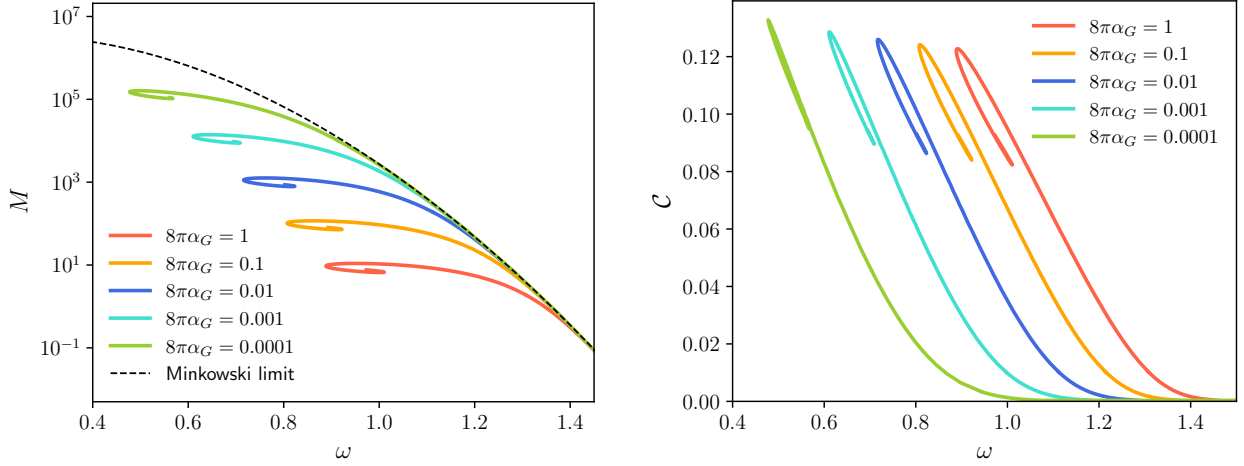


Figure 14. Sequence of spherical boson stars for the logarithmic potential with  $K = -0.1$ ,  $M$  being the dimensionless mass and  $C$  being the compactness. We see that  $M$  converges to the Q-ball solution in Eq. (62) as  $\alpha_G \rightarrow 0$ . In particular, for small values of  $\phi$  (low mass) the solutions approach the Minkowski case, where  $M$  decreases exponentially with frequency  $\omega$ .

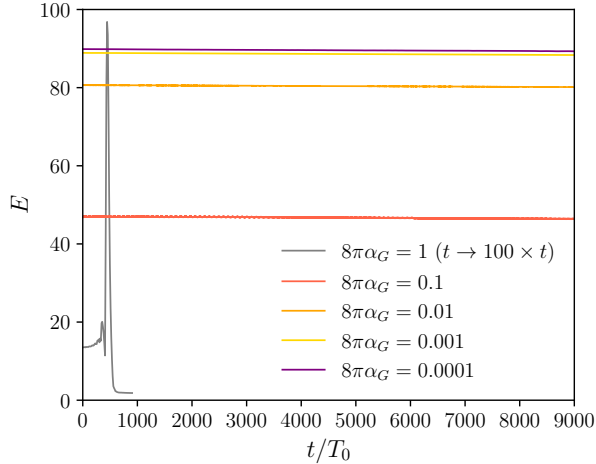


Figure 15. Charge-swapping configurations for the logarithmic potential with  $\omega = 1.2$ , prepared from a distance  $d = 2$  for different values of the gravitational coupling constant. The  $t$  axis for the  $8\pi\alpha_G = 1$  case is scaled by a factor of 100 in order to visualize its collapse.

cial dipolar contribution, and the Noether density has a dipolar structure that is oscillating. This resembles the energy density distribution of a scalar field configuration used previously as an alternative explanation [35] to solve the problem of the anisotropic distribution of satellite galaxies observed in the Milky Way, M31 and Centaurus A. Other explanations for the plane of satellite galaxies problem include using baryonic effects, combined gravitational distribution effects [103] and formation of satellite galaxies within the scalar field dark matter model [104]; see [71] for a review.

The plane of satellite galaxies problem arises from the distribution and motion of these galaxies in planes that

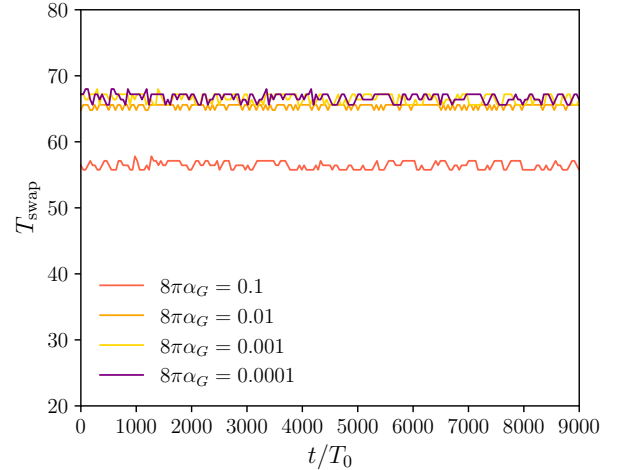


Figure 16. Charge-swapping period  $T_{\text{swap}}$  for the logarithmic charge-swapping boson stars in Fig. 15.

are perpendicular to the plane of their host galaxy. This is unnatural to explain in the cold dark matter paradigm, where the simulations predict that satellites should be isotropically distributed [105, 106]. The authors in [35] address this problem using multi-state solutions of a system of self-gravitating scalar fields in the Newtonian limit, composed of a spherical state and a dipolar state, which allow them to model dark matter halos and study the motion of test particles on top of the generated gravitational potential. They found that an anisotropic triaxial Navarro-Frenk-White halo does not lead to the orbital angular momenta of the satellites aligning with the equator, but the anisotropic (multi-state) scalar field halo does accommodate the particles in orbital planes close to the galactic poles. This is made possible because of the

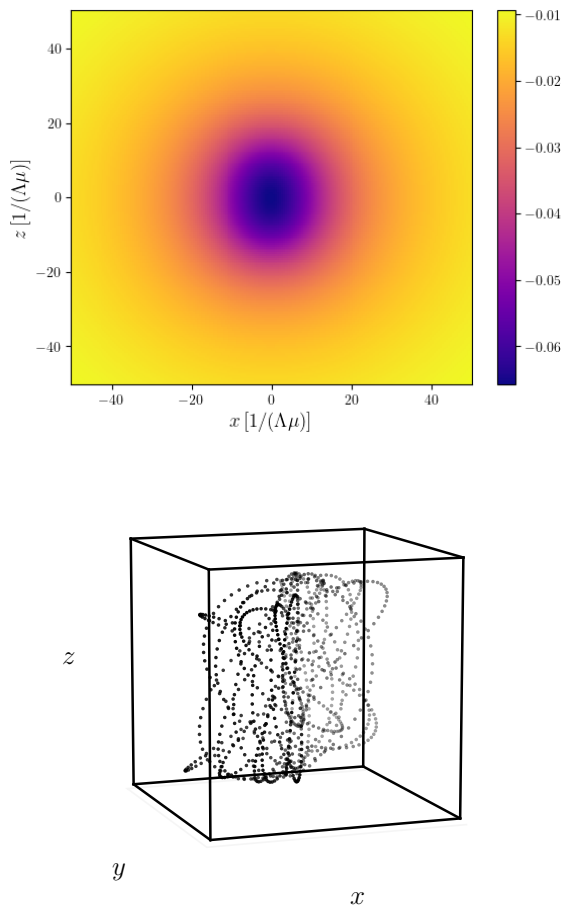


Figure 17. Newtonian gravitational potential  $\Lambda U$  of the dipolar charge-swapping configuration with  $\omega = 0.98$  (top) and motion of a single random “particle” up to  $t = 12\tau_s$  using 1000 steps of time (bottom).  $\tau_s$  is the time for a “particle” in the equatorial plane to complete a circular orbit.

specific morphology of the dipolar contribution, which is produced by a scalar field anti-symmetric with respect to the galactic plane.

The self-gravitating charge-swapping configurations in the case of a free scalar field or the scalar field with a logarithmic potential are extremely long-lived and have a morphology similar to the monopole dominating configuration of [35] (close to spherical symmetry but with a sizable dipolar contribution). More importantly, their constituent boson stars are close to the Newtonian regime, so these dipolar configurations are very dilute, fully compatible with cosmological constraints. In the following, we explore the possibility of utilizing charge-swapping configurations, which, as nonspherical halo distributions, could lead to the desired anisotropic distribution of satellite galaxies. For definiteness, we will focus on charge-swapping dipolar configurations whose constituents are mini-boson stars with  $\omega = 0.98$ .

In the non-relativistic limit, the Einstein-Klein-Gordon system Eqs. (12) and (13) reduce to the Schrödinger-Poisson system which is more tractable and also has addi-

tional re-scaling properties [107]. This approximation is valid when the scalar field is non-relativistic which in particular implies  $\phi \ll 1$ . So even in the presence of higher order polynomial self-interactions, the scalar equation of motion reduces to

$$i\partial_t\Psi_w = -\frac{1}{2}\nabla^2\Psi_w + U\Psi_w, \quad (65)$$

$$\nabla^2 U = 4\pi\alpha_G|\Psi_w|^2. \quad (66)$$

where

$$\Psi_w = \sqrt{2}\exp(it)\phi, \quad (67)$$

$U$  is the Newtonian gravitational potential, which can be extracted by comparing Eq. (19) with

$$ds^2 = -(1 + 2U)dt^2 + (1 - 2U)dr^2 + r^2d\Omega^2, \quad (68)$$

A consistency condition is that  $U \ll 1$ . We assume that the weak field and low energy regime is valid in the late universe. Boson stars are known to be in this limit when  $\omega$  is close to 1, where the compactness approaches 0.

Unlike the Einstein-Klein-Gordon system, the Schrödinger-Poisson equations have<sup>4</sup> the following scaling invariance:

$$(\Psi_w, U, x^i, t) \rightarrow (\Lambda^2\Psi_w, \Lambda^2U, \Lambda^{-1}x^i, \Lambda^{-2}t), \quad (69)$$

for any value of the real scaling constant  $\Lambda$ . This allows to obtain the full sequence of Newtonian boson stars once a single solution has been found, unlike the relativistic analogue, where the family of solutions, say, the one presented in Fig. 1, must be constructed numerically solving the equations at each point. This rescaling is independent of the rescaling used to obtain dimensionless quantities, so to recover the physical system, as in the relativistic case, we must choose a value of  $\mu$  as explained in Section II C. We have previously obtained the metrics in the full general relativistic formulation. For this application, it is sufficient to extract the non-relativistic limit from Eq. (67) and Eq. (68).

We choose to perform the analysis at a certain representative space slice with  $t = 4000T_0$  of the dipolar configuration with  $\omega = 0.98$  well within the charge-swapping stage. However, the results are insensitive to the specific time period chosen within this stage. To extract the 2D data at such time we use the *Kuibit* tool [108]. Based on the consistency statistical tests performed in [35], we choose the values of  $\mu$  and  $\Lambda$ , which completely fix the scale of the system, to be such that the size of the configuration, which has an equatorial radius of about 16 units, corresponds to a physical size of 300 kpc (radius encompassing the 11 classical satellites of the Milky Way [109]),

<sup>4</sup> Subject to the restrictions  $\phi \ll 1$  and  $U \ll 1$ . See Ref. [36] for the post-Newtonian expansion of the Einstein-Klein-Gordon system.

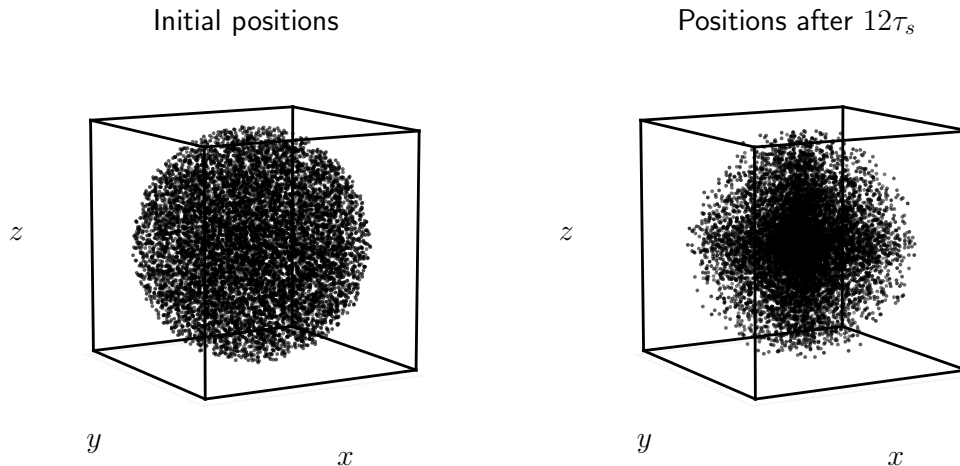


Figure 18. “Particles” in the configuration space moving in the (Newtonian) gravitational potential of a dipolar charge-swapping configuration in a free scalar model. The length of the cube’s side is  $2 \times 300$  kpc. The configuration that gives rise to the dark matter halo, on top of which “particles” are moving is a dilute dipolar configuration with  $\omega = 0.98$ . For reference, the radius of the constituent boson star in this scenario is  $\sim 600$  kpc and the formed complex boson star is about half the size of it.

together with the condition that the circular velocity of the stars in the galactic disk at a point 30kpc away from the galactic center is 100 km/s, implying similar contributions from the enclosed mass at radius  $r=30$ kpc of dark matter and baryonic matter. These two conditions lead to the values  $\mu\hbar \sim 10^{-25}$ eV and  $\Lambda = 0.01$ . The precise determination of these two parameters given the rotation curve of the Milky Way and a model for the galactic bulge and disc deserves a statistical analysis which is beyond the scope of this paper.

Next, we study the motion of  $10^4$  “particles” moving the gravitational field of  $U$ . After some time, the distribution of the “particles” reflects the probability of finding (idealized) satellite galaxies in the halo. To that end, we randomly place “particles” inside a sphere of radius  $R = 16/(\Lambda\mu)$ , corresponding to  $R = 300$ kpc (see the left panel of Fig. 18), and with velocities in random directions and magnitudes smaller than 1/4 of the escape velocity of a “particle” located in the equatorial plane at a distance  $R$  from the center of the galaxy:  $v < v_{\max} = \sqrt{U(R, 0, 0)}/8$ .

The “particles” are left to evolve. In Fig. 17, we show the gravitational potential and the motion of a single “particle” in it, in units of  $\mu$  and  $\Lambda$ , which specify the galactic sizes. This is possible because the equations of motion of the “particles” inherit the two scaling invariances of the Shrödinger-Poisson equations mentioned above. Similar to [35], we choose to evolve up to  $t = 12\tau_s$ , where  $\tau_s$  is defined as the time it takes for a particle in the equatorial plane to complete a circular orbit. After this, we restore units of every involved physical quantity.

From Fig. 18 and similar plots and projections at different times, we see that after several  $\tau_s$ , the distribution tends to a stationary non-spherical distribution in space,

and the distribution of the orientation of the satellite orbits is also stationary and anisotropic. This can be seen in Fig. 19. More importantly, we notice that the orbital angular momenta (known as the orbital pole in the astronomy literature) of the satellites, *i.e.*, the “particles” located between 30 and 300 kpc, are concentrated around the equator. Other choices of the maximum allowed value for the random magnitude of the velocity lead to similar results as long as it does not exceed 1/2 the escape velocity of the particle located in the equatorial plane at a distance  $R$  from the center. For a comparison, we have plotted the orbital poles of the 11 Milky Way classical satellites obtained from Ref. [109] together with the particle orbital poles at  $t = 12\tau_s$  in Fig. 20.

Let us comment on the robustness of the charge-swapping configurations for modeling dark matter halos. In our general relativistic numerical simulations, we find that the free-field charge-swapping configurations can be formed from quite generic initial setups and are attractor solutions in the dynamical evolution. Also, as mentioned in the introduction, they may initially be formed from fragmentation of some homogeneous condensate in the early universe. They live for extremely long times and are sufficiently stable in terms of modeling a galactic halo. To see this, note that for our case we have that the dimensionless timescale is  $\Lambda^2\mu\tau_s \sim 600$ , calculated from  $U$  according to its definition, which is much smaller than the (minimum) lifetime of the free-field charge-swapping configurations explored in Section III. For the values of  $\Lambda$  and  $\mu$  for this cosmological application we obtain,

$$\tau_s \sim 4 \text{ Gyrs}, \quad (70)$$

after restoring units. Meaning that the angular distribution of the angular momenta is already oriented toward the

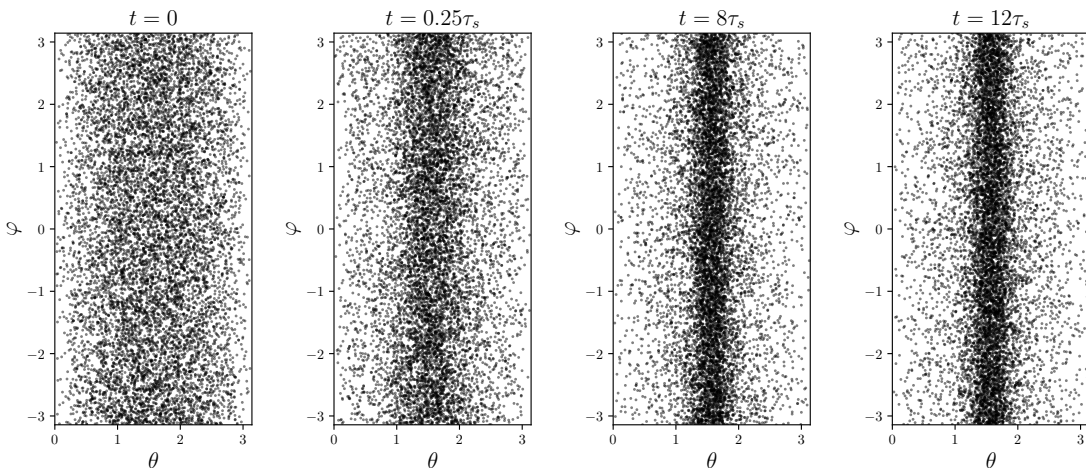


Figure 19. Angular distribution of the angular momenta of  $10^4$  “particles” for the fiducial dipolar charge-swapping configuration. The initial distribution is isotropic, and it quickly relaxes to a configuration where the tangent of the orbital poles are oriented toward the galactic plane  $\theta = \pi/2$ . We only include particles within  $\Lambda\mu R \in (0.16, 16)$  which takes into account “particles” with  $R > 30$  kpc, the size of the Milky Way stellar disc.

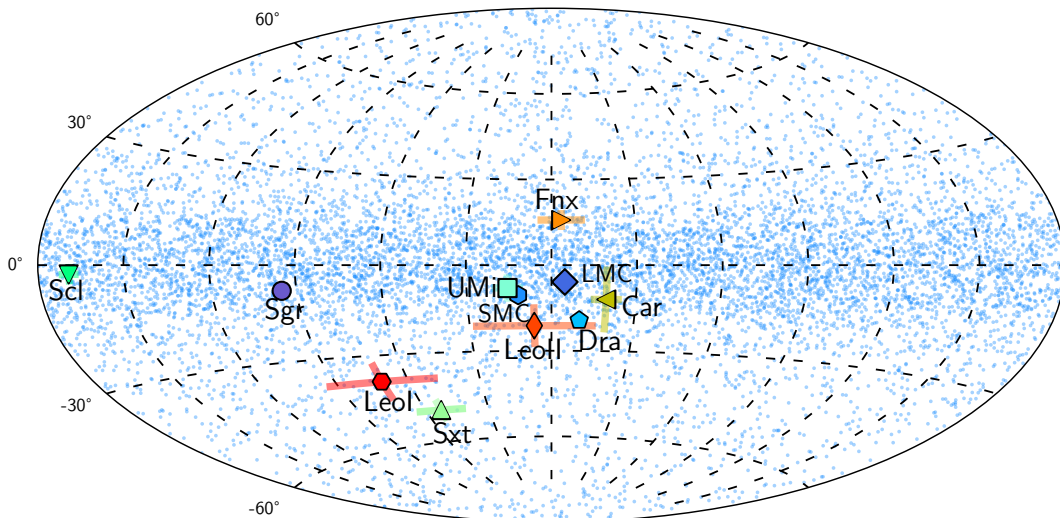


Figure 20. Orbital poles and their uncertainty of the 11 Milky Way classical satellites. Here the angles correspond to the Galactic longitude and latitude. The thick color lines correspond to the error bars in both angles for each satellite, arising from the uncertainty in determining the velocity components of the galaxies. The blue dots in the background correspond to the  $10^4$  “particles” at  $t = 12\tau$  of Fig. 19.

galactic pole after 1 Gyr (as can be seen in Fig. 19) and that the charge-swapping configurations live for much longer than is required for the galactic halos in the Universe.

Furthermore, it is possible that the gravitational potential in this scenario could destroy the Galactic disc. To see that this does not happen, we place “particles” in a disk of radius 30 kpc with a small thickness varying between 0 and 10 percent of the disk radius. We give initial velocities to the “particles” with directions parallel to the equatorial plane and with velocities such that they would follow perfect circular motion if they were lo-

cated in their positions projected in the equatorial plane. Then, we let them evolve for  $12\tau_s$ . We find that within the chosen parameters the structure of the disc does not change: its radius and thickness remain the same, as can be seen in Fig. 21

## VI. CONCLUSIONS

In this paper, we have discussed the complex structures of boson stars and established the existence of charge-swapping configurations in the presence of gravity. We

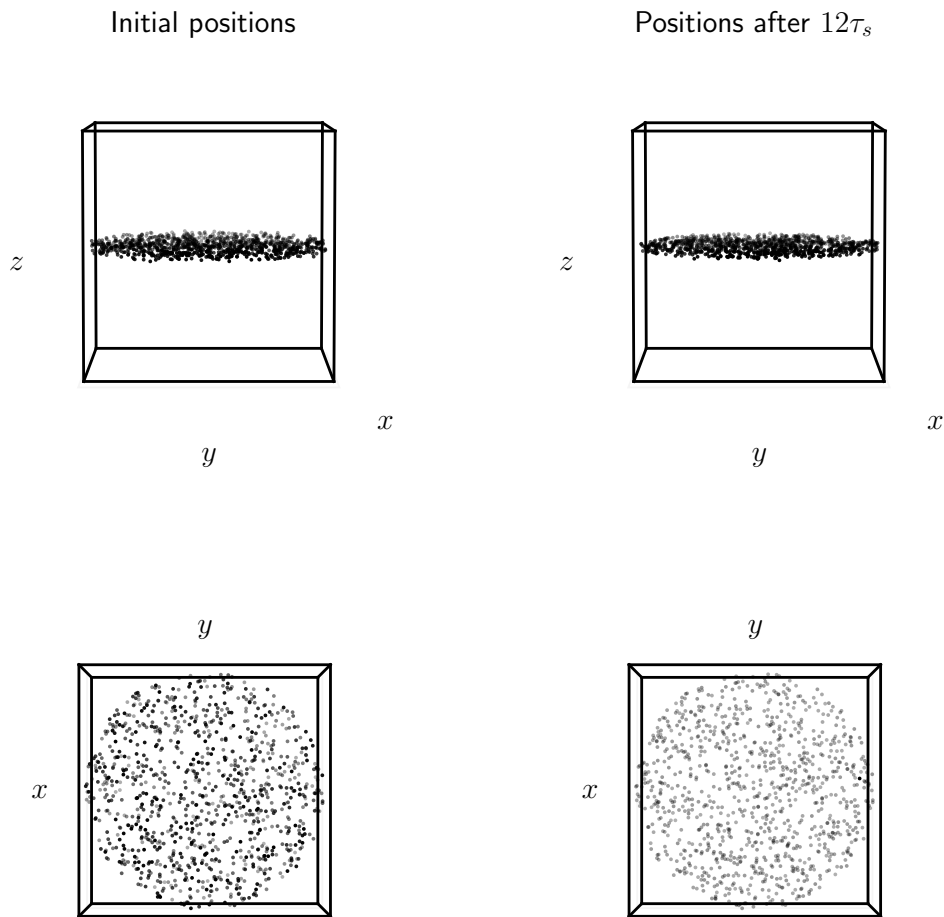


Figure 21. “Particles” in a disc of radius 30 kpc and thickness 3 kpc moving in a (Newtonian) gravitational potential of the fiducial dipolar configuration (see Fig. 18). The side of the cube is of length 60 kpc. The bottom panels display a top-view of the disc.

have shown how the metric field changes the stability and other properties of the charge-swapping configurations and recovered the Minkowski flat results in suitable limits. Particularly, the quadratic monomial potential, the sextic polynomial potential and the running mass/logarithmic potential are explored with fully non-linear numerical relativity simulations. For the quadratic and logarithmic case, the complex boson stars are found to be very stable, and we have yet to see them decay in our long-term simulations. The existence of charge-swapping configurations for the quadratic potential is a novelty when coupling the U(1) scalar to gravity, thanks to the gravitational attractions.

In the free scalar case, taking the dipolar boson star for example, we have found that the real and imaginary parts of the scalar field oscillate with slightly different frequencies. This difference determines the main frequency at

which the Noether charge of the two components of the system is exchanged. Also, we have found that configurations can avoid gravitational collapse when the initial stars are prepared with sufficiently low masses and separations, as any excess energy is radiated in the initial relaxation stage. In the sextic potential case, we have found evidence of transient existence of compact self-gravitating charge-swapping configurations. Although defining compactness in the case of dynamical configurations is not straightforward, we found that charge-swapping configurations prepared with boson stars with  $C \sim 0.1$ , some transient configurations emerge after losing about half of their mass (Fig. 13). These resulting structures maintain roughly the same radius as the initial stars, rendering the newly formed configurations compact. Thus, a low scalar field density is not a requirement for the existence of these configurations.

Finally, we have proposed a concrete application for these charge-swapping configurations at large/galactic scales. Assuming that the Galactic dark matter halo is a charge-swapping dipole, we have shown that test particles placed on it will cluster anisotropically and particularly their angular momenta will be oriented in the direction of the Galactic plane. This is different from the scenario of the cold dark matter model where an isotropic halo is more likely to be formed. We have chosen the model parameters to preliminarily fit the observations in the Milky Way, but a precise determination of the model parameters requires a statistical consistency analysis, which is beyond the scope of the current paper.

A particular extension of the current work is to study the gravitational signals associated with the relaxation period, after, say, a collision, and the decay or collapse of the most compact charge-swapping configurations, which is also left for future work.

## ACKNOWLEDGMENTS

We would like to thank Qi-Xin Xie for helpful discussions. SYZ acknowledges support from the National Key R&D Program of China under grant No. 2022YFC2204603 and from the National Natural Science Foundation of China under grant No. 12075233 and 12247103.

## Appendix: Convergence tests

The charge-swapping configurations found in this work are very long-lived, so convergence tests of the numerical code are very important. First, we have checked the consistency of the full implementation by constructing and evolving isolated stable boson stars that are previously known, calculating the frequency of the scalar field during the simulation and checking whether it coincides with the frequency of the stationary solution for a long period of time,  $t \sim 10^4$ . The coordinates chosen are such that the different metric functions are expected to stay static during the evolution, which we again verify by plotting the global minima and maxima of some of them. To evaluate the consistency of the charge-swapping dynamics, we have compared with the flat spacetime results in [64] for the polynomial potential case and [66] for the logarithmic potential. Specifically, we compared the curves of  $E$  and found good agreement despite the fact that the implementation is completely different.

In Fig. 22, we show the Noether charge for different sizes of the physical box and spatial resolutions. In this plot we have plotted the time window between  $t = 3000$  and  $t = 3400$  to make convergence readily apparent, however the following conclusions can be obtained from other time windows. We see that the medium and high resolutions provide precise results. The same applies to the two bigger box cases, with  $x_{\max}^i = 160$  and  $320$ , but the three

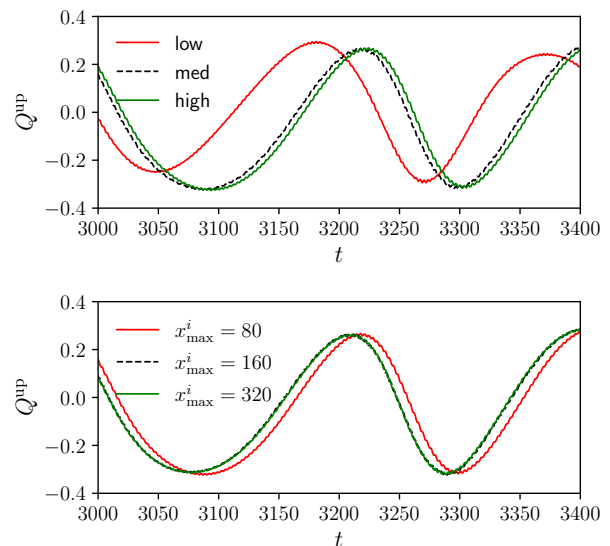


Figure 22. Resolution comparison for the charge  $Q^{\text{up}}$  for resolutions in the finest refinement grid corresponding to  $\Delta x^i = 0.8, 0.4$  and  $0.2$  (top panel) and different physical box sizes (bottom). For the resolution comparison, we use a box size of  $160^3$ , while for the size comparison we use the medium resolution. The configuration corresponds to the free field dipole with  $\omega = 0.97$  and  $d = 24$ .

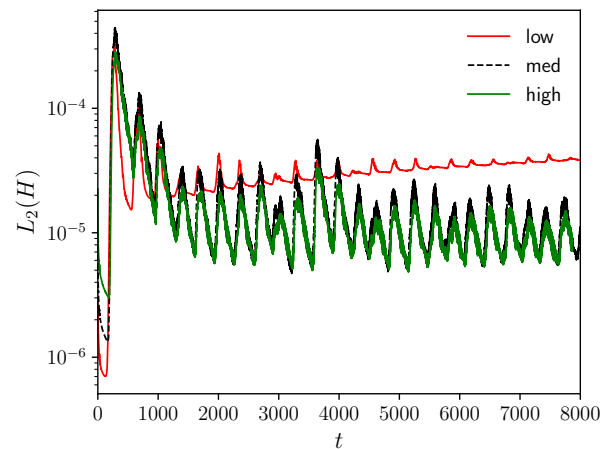


Figure 23. Convergence behavior of the Hamiltonian constraint violation for the same case described in Fig. 22.

box sizes are in good agreement for the amplitudes, and the frequencies of the charge oscillations differ from each other only by a phase. In our simulations of the dipolar free field case, we used the medium resolution and the smaller box size. In Fig. 23 we show the  $L_2$ -norm of the Hamiltonian constraint Eq. 24. The violation of this constraint begins from small values and increases in the initial relaxation stage. The errors reduce by one order of magnitude for the medium and high resolutions. If we start with different values of  $d$  or start with different models of initial boson stars the violation of the

constrains (at least in the medium resolution) is of the same order as the one showed in Fig. 23 whenever the configuration do not collapse. For instance, for smaller separations, the constraint violations remain of the same order within a certain range of closely spaced configurations, provided they do not collapse. However, in configurations with initially larger separations, the quantities  $H$  and  $\mathcal{M}_i$  become more pronounced during the initial relaxation stage.

Finally we comment on the momentum constraint. We have tracked the evolution of it and found that the components  $L_2(\mathcal{M}_x)$  and  $L_2(\mathcal{M}_y)$  exhibit the same qualitative behavior as the Hamiltonian evolution shown in Fig. 23. The maximum occurs at the beginning of the initial relaxation process, followed by some dissipation of the numerical error. Both components are an order of magnitude smaller than the Hamiltonian and the  $L_2(\mathcal{M}_z)$  component is approximately half the size of the  $x$  and  $y$  components.

- 
- [1] D. J. Kaup, *Phys. Rev.* **172**, 1331 (1968).
- [2] M. Colpi, S. L. Shapiro, and I. Wasserman, *Phys. Rev. Lett.* **57**, 2485 (1986).
- [3] R. Friedberg, T. D. Lee, and Y. Pang, *Phys. Rev. D* **35**, 3658 (1987).
- [4] P. Jetzer and J. J. van der Bij, *Phys. Lett. B* **227**, 341 (1989).
- [5] C. A. R. Herdeiro and E. Radu, *Phys. Rev. Lett.* **112**, 221101 (2014), arXiv:1403.2757 [gr-qc].
- [6] R. Brito, V. Cardoso, C. A. R. Herdeiro, and E. Radu, *Phys. Lett. B* **752**, 291 (2016), arXiv:1508.05395 [gr-qc].
- [7] S. L. Liebling and C. Palenzuela, *Living Rev. Rel.* **26**, 1 (2023), arXiv:1202.5809 [gr-qc].
- [8] H.-Y. Zhang, (2024), arXiv:2406.05031 [hep-ph].
- [9] E. Seidel and W.-M. Suen, *Phys. Rev. D* **42**, 384 (1990).
- [10] J. Balakrishna, E. Sfeidel, and W.-M. Suen, *Phys. Rev. D* **58**, 104004 (1998), arXiv:gr-qc/9712064.
- [11] E. Seidel and W.-M. Suen, *Phys. Rev. Lett.* **72**, 2516 (1994), arXiv:gr-qc/9309015.
- [12] M. Bezares, C. Palenzuela, and C. Bona, *Phys. Rev. D* **95**, 124005 (2017), arXiv:1705.01071 [gr-qc].
- [13] N. Sanchis-Gual, C. Herdeiro, and E. Radu, *Class. Quant. Grav.* **39**, 064001 (2022), arXiv:2110.03000 [gr-qc].
- [14] V. Jaramillo, N. Sanchis-Gual, J. Barranco, A. Bernal, J. C. Degollado, C. Herdeiro, and D. Núñez, *Phys. Rev. D* **101**, 124020 (2020), arXiv:2004.08459 [gr-qc].
- [15] N. Sanchis-Gual, F. Di Giovanni, C. Herdeiro, E. Radu, and J. A. Font, *Phys. Rev. Lett.* **126**, 241105 (2021), arXiv:2103.12136 [gr-qc].
- [16] M. Bezares and C. Palenzuela, *Class. Quant. Grav.* **35**, 234002 (2018), arXiv:1808.10732 [gr-qc].
- [17] R. Croft, T. Helfer, B.-X. Ge, M. Radia, T. Evstafyeva, E. A. Lim, U. Sperhake, and K. Clough, *Class. Quant. Grav.* **40**, 065001 (2023), arXiv:2207.05690 [gr-qc].
- [18] F. Atteneder, H. R. Rüter, D. Cors, R. Rosca-Mead, D. Hilditch, and B. Brügmann, *Phys. Rev. D* **109**, 044058 (2024), arXiv:2311.16251 [gr-qc].
- [19] N. Sanchis-Gual, C. Herdeiro, J. A. Font, E. Radu, and F. Di Giovanni, *Phys. Rev. D* **99**, 024017 (2019), arXiv:1806.07779 [gr-qc].
- [20] T. Helfer, U. Sperhake, R. Croft, M. Radia, B.-X. Ge, and E. A. Lim, *Class. Quant. Grav.* **39**, 074001 (2022), arXiv:2108.11995 [gr-qc].
- [21] C. Palenzuela, I. Olabarrieta, L. Lehner, and S. L. Liebling, *Phys. Rev. D* **75**, 064005 (2007), arXiv:gr-qc/0612067.
- [22] M. Gleiser and R. Watkins, *Nucl. Phys. B* **319**, 733 (1989).
- [23] P. V. P. Cunha, J. A. Font, C. Herdeiro, E. Radu, N. Sanchis-Gual, and M. Zilhão, *Phys. Rev. D* **96**, 104040 (2017), arXiv:1709.06118 [gr-qc].
- [24] B. Kleihaus, J. Kunz, and S. Schneider, *Phys. Rev. D* **85**, 024045 (2012), arXiv:1109.5858 [gr-qc].
- [25] T. Tamaki and N. Sakai, *Phys. Rev. D* **81**, 124041 (2010), arXiv:1105.1498 [gr-qc].
- [26] H.-B. Li, S. Sun, T.-T. Hu, Y. Song, and Y.-Q. Wang, *Phys. Rev. D* **101**, 044017 (2020), arXiv:1906.00420 [gr-qc].
- [27] H. Olivares, Z. Younsi, C. M. Fromm, M. De Laurentis, O. Porth, Y. Mizuno, H. Falcke, M. Kramer, and L. Rezzolla, *Mon. Not. Roy. Astron. Soc.* **497**, 521 (2020), arXiv:1809.08682 [gr-qc].
- [28] P. Amaro-Seoane, J. Barranco, A. Bernal, and L. Rezzolla, *JCAP* **11**, 002 (2010), arXiv:1009.0019 [astro-ph.CO].
- [29] A. Bernal and F. Siddhartha Guzman, *Phys. Rev. D* **74**, 103002 (2006), arXiv:astro-ph/0610682.
- [30] P. Grandclement, C. Somé, and E.ourgoulhon, *Phys. Rev. D* **90**, 024068 (2014), arXiv:1405.4837 [gr-qc].
- [31] A. Suárez, V. H. Robles, and T. Matos, *Astrophys. Space Sci. Proc.* **38**, 107 (2014), arXiv:1302.0903 [astro-ph.CO].
- [32] L. Hui, J. P. Ostriker, S. Tremaine, and E. Witten, *Phys. Rev. D* **95**, 043541 (2017), arXiv:1610.08297 [astro-ph.CO].
- [33] V. Jaramillo and D. Núñez, *Phys. Rev. D* **106**, 104023 (2022), arXiv:2209.07549 [gr-qc].
- [34] G. Choi, H.-J. He, and E. D. Schiappacasse, *JCAP* **10**, 043 (2019), arXiv:1906.02094 [astro-ph.CO].
- [35] J. Solís-López, F. S. Guzmán, T. Matos, V. H. Robles, and L. A. Ureña López, *Phys. Rev. D* **103**, 083535 (2021), arXiv:1912.09660 [astro-ph.GA].
- [36] L. Annulli, V. Cardoso, and R. Vicente, *Phys. Rev. D* **102**, 063022 (2020), arXiv:2009.00012 [gr-qc].
- [37] F. S. Guzman and L. A. Ureña-Lopez, *Astrophys. J.* **645**, 814 (2006), arXiv:astro-ph/0603613.
- [38] F. S. Guzman and J. M. Rueda-Becerril, *Phys. Rev. D* **80**, 084023 (2009), arXiv:1009.1250 [astro-ph.HE].
- [39] Y.-B. Zeng, S.-Y. Cui, H.-B. Li, S.-X. Sun, Y.-P. Zhang, and Y.-Q. Wang, *Eur. Phys. J. C* **84**, 187 (2024), arXiv:2103.10717 [gr-qc].
- [40] J. a. L. Rosa and D. Rubiera-Garcia, *Phys. Rev. D* **106**, 084004 (2022), arXiv:2204.12949 [gr-qc].
- [41] J. a. L. Rosa, C. F. B. Macedo, and D. Rubiera-Garcia, *Phys. Rev. D* **108**, 044021 (2023), arXiv:2303.17296 [gr-qc].
- [42] T. Bernal and T. Matos, (2024), arXiv:2407.05273

- [astro-ph.GA].
- [43] S. Yoshida and Y. Eriguchi, *Phys. Rev. D* **56**, 762 (1997).
- [44] N. Sanchis-Gual, F. Di Giovanni, M. Zilhão, C. Herdeiro, P. Cerdá-Durán, J. A. Font, and E. Radu, *Phys. Rev. Lett.* **123**, 221101 (2019), arXiv:1907.12565 [gr-qc].
- [45] F. Di Giovanni, N. Sanchis-Gual, P. Cerdá-Durán, M. Zilhão, C. Herdeiro, J. A. Font, and E. Radu, *Phys. Rev. D* **102**, 124009 (2020), arXiv:2010.05845 [gr-qc].
- [46] N. Siemonsen and W. E. East, *Phys. Rev. D* **103**, 044022 (2021), arXiv:2011.08247 [gr-qc].
- [47] S. Yoshida and Y. Eriguchi, *Phys. Rev. D* **55**, 1994 (1997).
- [48] P. Cunha, C. Herdeiro, E. Radu, and Y. Shnir, *Phys. Rev. D* **106**, 124039 (2022), arXiv:2210.01833 [gr-qc].
- [49] C. A. R. Herdeiro and E. Radu, *Phys. Rev. Lett.* **131**, 121401 (2023), arXiv:2305.15467 [gr-qc].
- [50] P. Ildefonso, M. Zilhão, C. Herdeiro, E. Radu, and N. M. Santos, *Phys. Rev. D* **108**, 064011 (2023), arXiv:2307.00044 [gr-qc].
- [51] C. A. R. Herdeiro, J. Kunz, I. Perapechka, E. Radu, and Y. Shnir, *Phys. Rev. D* **103**, 065009 (2021), arXiv:2101.06442 [gr-qc].
- [52] R. Gervalle, *Phys. Rev. D* **105**, 124052 (2022), arXiv:2206.03982 [gr-qc].
- [53] S.-X. Sun, L. Zhao, and Y.-Q. Wang, *JHEP* **08**, 152 (2023), arXiv:2210.09265 [gr-qc].
- [54] S.-X. Sun and Y.-Q. Wang, (2023), arXiv:2312.16921 [gr-qc].
- [55] C. A. R. Herdeiro, J. Kunz, I. Perapechka, E. Radu, and Y. Shnir, *Phys. Lett. B* **812**, 136027 (2021), arXiv:2008.10608 [gr-qc].
- [56] M. Choquik, R. Masachs, and B. Way, *Phys. Rev. Lett.* **123**, 131101 (2019), arXiv:1904.02168 [gr-qc].
- [57] A. Bernal, J. Barranco, D. Alic, and C. Palenzuela, *Phys. Rev. D* **81**, 044031 (2010), arXiv:0908.2435 [gr-qc].
- [58] M. Alcubierre, J. Barranco, A. Bernal, J. C. Degollado, A. Diez-Tejedor, M. Megevand, D. Nunez, and O. Sarbach, *Class. Quant. Grav.* **35**, 19LT01 (2018), arXiv:1805.11488 [gr-qc].
- [59] F. S. Guzmán and L. A. Ureña López, *Phys. Rev. D* **101**, 081302 (2020), arXiv:1912.10585 [astro-ph.GA].
- [60] R. Friedberg, T. D. Lee, and A. Sirlin, *Phys. Rev. D* **13**, 2739 (1976).
- [61] S. R. Coleman, *Nucl. Phys. B* **262**, 263 (1985), [Addendum: *Nucl. Phys. B* 269, 744 (1986)].
- [62] T. D. Lee and Y. Pang, *Phys. Rept.* **221**, 251 (1992).
- [63] E. J. Copeland, P. M. Saffin, and S.-Y. Zhou, *Phys. Rev. Lett.* **113**, 231603 (2014), arXiv:1409.3232 [hep-th].
- [64] Q.-X. Xie, P. M. Saffin, and S.-Y. Zhou, *JHEP* **07**, 062 (2021), arXiv:2101.06988 [hep-th].
- [65] Q.-X. Xie, P. M. Saffin, A. Tranberg, and S.-Y. Zhou, *JHEP* **01**, 165 (2024), arXiv:2312.01139 [hep-th].
- [66] S.-Y. Zhou, P. M. Saffin, Q.-X. Xie, and S.-Y. Zhou, *JHEP* **07**, 060 (2022), arXiv:2202.08392 [hep-ph].
- [67] S.-Y. Zhou, *JCAP* **06**, 033 (2015), arXiv:1501.01217 [astro-ph.CO].
- [68] P. M. Saffin, Q.-X. Xie, and S.-Y. Zhou, *Phys. Rev. Lett.* **131**, 111601 (2023), arXiv:2212.03269 [hep-th].
- [69] V. Cardoso, R. Vicente, and Z. Zhong, *Phys. Rev. Lett.* **131**, 111602 (2023), arXiv:2307.13734 [hep-th].
- [70] H.-Y. Gao, P. M. Saffin, Y.-J. Wang, Q.-X. Xie, and S.-Y. Zhou, *Sci. China Phys. Mech. Astron.* **67**, 260413 (2024), arXiv:2306.01868 [gr-qc].
- [71] M. S. Pawłowski, *Galaxies* **9**, 66 (2021), arXiv:2109.02654 [astro-ph.GA].
- [72] R. Ruffini and S. Bonazzola, *Phys. Rev.* **187**, 1767 (1969).
- [73] C. A. R. Herdeiro, J. a. M. S. Oliveira, A. M. Pombo, and E. Radu, *Phys. Rev. D* **106**, 024054 (2022), arXiv:2206.02813 [gr-qc].
- [74] V. Jaramillo, N. Sanchis-Gual, J. Barranco, A. Bernal, J. C. Degollado, C. Herdeiro, M. Megevand, and D. Núñez, *Phys. Rev. D* **105**, 104057 (2022), arXiv:2202.00696 [gr-qc].
- [75] T. Nakamura, K. Oohara, and Y. Kojima, *Prog. Theor. Phys. Suppl.* **90**, 1 (1987).
- [76] M. Shibata and T. Nakamura, *Phys. Rev. D* **52**, 5428 (1995).
- [77] T. W. Baumgarte and S. L. Shapiro, *Phys. Rev. D* **59**, 024007 (1998), arXiv:gr-qc/9810065.
- [78] M. Alcubierre, *Introduction to 3+1 Numerical Relativity*, International Series of Monographs on Physics (OUP Oxford, 2008).
- [79] M. Alcubierre, J. Barranco, A. Bernal, J. C. Degollado, A. Diez-Tejedor, V. Jaramillo, M. Megevand, D. Núñez, and O. Sarbach, *Class. Quant. Grav.* **39**, 094001 (2022), arXiv:2112.04529 [gr-qc].
- [80] E.ourgoulhon, in *CompStar 2010: School and Workshop on Computational Tools for Compact Star Astrophysics* (2010) arXiv:1003.5015 [gr-qc].
- [81] V. Jaramillo, E. Jiménez-Vázquez, and D. Núñez, *Phys. Rev. D* **107**, 064061 (2023), arXiv:2302.07889 [gr-qc].
- [82] N. Siemonsen and W. E. East, *Phys. Rev. D* **108**, 124015 (2023), arXiv:2306.17265 [gr-qc].
- [83] T. Evstafyeva, U. Sperhake, T. Helfer, R. Croft, M. Raddia, B.-X. Ge, and E. A. Lim, *Class. Quant. Grav.* **40**, 085009 (2023), arXiv:2212.08023 [gr-qc].
- [84] P. Grandclement, “Kadath library,” (2009).
- [85] P. Grandclement, *J. Comput. Phys.* **229**, 3334 (2010), arXiv:0909.1228 [gr-qc].
- [86] “The einstein toolkit,” (2023).
- [87] F. Löffler *et al.*, *Class. Quant. Grav.* **29**, 115001 (2012), arXiv:1111.3344 [gr-qc].
- [88] J. D. Brown, P. Diener, O. Sarbach, E. Schnetter, and M. Tiglio, *Phys. Rev. D* **79**, 044023 (2009), arXiv:0809.3533 [gr-qc].
- [89] H. Witek, M. Zilhao, G. Bozzola, M. Elley, G. Ficarra, T. Ikeda, N. Sanchis-Gual, and H. Silva, “Canuda: a public numerical relativity library to probe fundamental physics,” (2021).
- [90] J. Thornburg, *Class. Quant. Grav.* **21**, 743 (2004), arXiv:gr-qc/0306056.
- [91] E. Schnetter, S. H. Hawley, and I. Hawke, *Class. Quant. Grav.* **21**, 1465 (2004), arXiv:gr-qc/0310042.
- [92] M. Alcubierre, B. Bruegmann, P. Diener, M. Koppitz, D. Pollney, E. Seidel, and R. Takahashi, *Phys. Rev. D* **67**, 084023 (2003), arXiv:gr-qc/0206072.
- [93] C. Bona, J. Masso, E. Seidel, and J. Stela, *Phys. Rev. Lett.* **75**, 600 (1995), arXiv:gr-qc/9412071.
- [94] E. Seidel and W. M. Suen, *Phys. Rev. Lett.* **66**, 1659 (1991).
- [95] H.-Y. Zhang, M. Jain, and M. A. Amin, *Phys. Rev. D* **105**, 096037 (2022), arXiv:2111.08700 [astro-ph.CO].
- [96] Y.-J. Wang, Q.-X. Xie, and S.-Y. Zhou, *Phys. Rev. D*

- 108**, 025006 (2023), [arXiv:2210.04969 \[hep-th\]](#).
- [97] K. Enqvist and J. McDonald, *Phys. Lett. B* **425**, 309 (1998), [arXiv:hep-ph/9711514](#).
- [98] K. Enqvist and J. McDonald, *Nucl. Phys. B* **538**, 321 (1999), [arXiv:hep-ph/9803380](#).
- [99] K. Enqvist and J. McDonald, *Nucl. Phys. B* **570**, 407 (2000), [Erratum: *Nucl.Phys.B* 582, 763–763 (2000)], [arXiv:hep-ph/9908316](#).
- [100] T. Multamaki and I. Vilja, *Nucl. Phys. B* **574**, 130 (2000), [arXiv:hep-ph/9908446](#).
- [101] K. Enqvist, A. Jokinen, and J. McDonald, *Phys. Lett. B* **483**, 191 (2000), [arXiv:hep-ph/0004050](#).
- [102] S. Kasuya and M. Kawasaki, *Phys. Rev. D* **62**, 023512 (2000), [arXiv:hep-ph/0002285](#).
- [103] T. Sawala, M. Cautun, C. S. Frenk, J. Helly, J. Jasche, A. Jenkins, P. H. Johansson, G. Lavaux, S. McAlpine, and M. Schaller, *Nature Astron.* **7**, 481 (2023), [arXiv:2205.02860 \[astro-ph.GA\]](#).
- [104] S. Park, D. Bak, J.-W. Lee, and I. Park, *JCAP* **12**, 033 (2022), [arXiv:2207.07192 \[astro-ph.CO\]](#).
- [105] E. J. Shaya and R. B. Tully, *Mon. Not. Roy. Astron. Soc.* **436**, 2096 (2013), [arXiv:1307.4297 \[astro-ph.CO\]](#).
- [106] M. S. Pawlowski, *Mod. Phys. Lett. A* **33**, 1830004 (2018), [arXiv:1802.02579 \[astro-ph.GA\]](#).
- [107] V. Jaramillo, *Weak field limit of a self-gravitating scalar field*, Master's thesis, Universidad Nacional Autónoma de México (2019).
- [108] G. Bozzola, *J. Open Source Softw.* **6**, 3099 (2021), [arXiv:2104.06376 \[gr-qc\]](#).
- [109] M. S. Pawlowski and P. Kroupa, *Mon. Not. Roy. Astron. Soc.* **491**, 3042 (2020), [arXiv:1911.05081 \[astro-ph.GA\]](#).